



Student Research Project

Determination of a Fit Function for the Critical Current Density for NbTi Cables used in LHC Main Bending Magnets

Nikolai Schwerg

Geneva, January 2005

Supervisors:

- **Dr.-Ing. Christine Völlinger**
AT-MAS-MA-group, CERN European Organization for Nuclear Research,
Geneva
- **Prof. Dr.-Ing. Heino Henke**
Institute for Technical Computer Science and Microelectronics,
Department of Theoretical Electrical Engineering, Technical University,
Berlin



Abstract

For the construction of the LHC [12] at CERN the main dipoles and the superconducting cables are produced in industry. As part of the quality control the field quality of the magnets is measured both at warm and at cold conditions at CERN. In superconducting accelerator magnets field errors are mainly created by the positioning of the conductors, but also by so-called persistent currents.

These currents are linked to the superconductor magnetization and they are an inevitable property of type II superconducting materials. The superconductor magnetization behavior of each strand used for the LHC main dipoles is tested at CERN and the cable has to be approved before use. It has been observed that the dependency of the superconductor magnetization on the applied magnetic induction is different for the different manufacturers.

Based on the magnetization measurements and the critical state model [1] the persistent current effects can be calculated by means of a model for superconducting filaments. For this thesis the intersecting ellipse model [19] is used which is implemented in the CERN field computation program ROXIE [15] and is used for the calculation of the expected field errors in the LHC magnets.

In this work a new fit function for the critical current density of NbTi cables for the LHC main dipoles is presented. This newly developed fit function is used as input for the existing sc model and complete magnet cross-sections have been calculated. The simulation results have been compared with measurements at cold of the LHC main dipoles. A very good agreement with measurements for small and intermediate field values could be observed.

Acknowledgement

The work presented in this thesis has been carried out in the framework of the Technical Student Program at CERN in the AT-MAS group. I am most grateful to my supervisor at CERN, Dr.-Ing. Christine Völlinger for her support, for fruitful discussions and for giving me the opportunity to carry out this thesis work.

I am very glad that she helped with the technical writing and that she patiently corrected my English.

Furthermore I want to thank her for helping me to settle down in Geneva and at CERN. By sharing her professional experiences she gave me very useful advices for my future and the development of my career.

I would be very happy continuing our good collaboration!

I wish to give acknowledgements to Dr.-Ing habil. Stephan Russenschuck from CERN for the help with the simulation program ROXIE and for being available for numerous discussions.

I very much appreciated the work in the AT-MAS group and want to thank all my colleagues for the pleasant atmosphere during my stay.

I like to thank Prof. Dr.-Ing. Heino Henke from Technical University of Berlin for his help with my application at CERN and his two visits during my stay.

Further I want to express my gratitude to Dr.-Ing. Manfred Filtz from the Technical University of Berlin for his willingness to be ready to listen and for keeping the spirits up.

I thank my family for their unlimited support and help during my stay in Geneva.

At last I thank my love Jelena not only standing the separation but encouraging me to take the opportunity to work at CERN.

Contents

List of Tables	vii
List of Figures	viii
1 Introduction	1
1.1 Aim of the Work	1
1.2 Outline of this Thesis	1
1.3 The Large Hadron Collider	2
1.4 Superconducting Magnets	3
1.4.1 LHC Main Bending Magnets	4
1.4.2 Cable for the LHC Main Dipole Magnets	6
2 Basics	9
2.1 Superconductivity	9
2.2 Model of a Hard Superconductor	11
2.2.1 Critical State Model	12
2.2.2 The Wilson Model	15
2.2.3 The Intersecting Ellipse Model	15
2.3 Field Errors	22
2.3.1 Multipole Expansion	22
2.3.2 Geometric Field Error	24
2.3.3 Persistent Current Field Errors	26
2.4 The Simulation Program ROXIE	28
2.5 Superconductor Magnetization	30
2.5.1 Measurement of Superconductor Strand Magnetization	30
2.5.2 Superconductor Magnetization for Different Manufacturers	32
2.5.3 Conversion of Superconductor Magnetization	33
2.6 Cold Measurement of Magnets	35
2.6.1 The Field Quality Measurement	36
2.6.2 Current Ramp Cycle	36

3	Fit Function for the Critical Current Density	38
3.1	Scaling Power Law	39
3.1.1	State of the Art	40
3.1.2	Analysis of Sensitivity	43
3.1.3	Adapting Parameters to Different Cables	45
3.1.4	Unphysical Behavior	47
3.2	Fixed Ending	51
3.3	No Pinch Off	53
3.4	Double Bending Function	56
4	Conclusion and Outlook	61
4.1	Conclusion	61
4.2	Outlook	62
	Bibliography	64
A	Intersecting Circles	66
B	Mathematical Tools	68
B.1	Standard Deviation	68
B.2	Linear Regression	68

List of Tables

1.1	Number of magnets produced with each cross section layout	5
1.2	LHC Cable Data.	8
1.3	Number of magnets produced with each cable combination.	8
3.1	Parameter range and values for the scaling power law by L. Bottura. . . .	39
3.2	Parameters of Summers' approach in terms of the scaling power law. . . .	40
3.3	Parameters for the unspecific fit by Völlinger.	40
3.4	Parameters and standard deviation for specific scaling power law.	46
3.5	Parameters and standard deviation for scaling power law with fixed ending.	51
3.6	Parameters and standard deviation for scaling power law without pinch off.	54
3.7	Parameters and standard deviation for the double bending function.	57

List of Figures

1.1	LHC tunnel after completion with dipole magnets (blue).	3
1.2	Ideal dipole and quadrupole fields.	4
1.3	Cross section of the LHC main dipole magnet.	5
1.4	Exploded view of an LHC main dipole.	6
1.5	Sketch of the an LHC main dipole.	7
1.6	Cable for LHC main dipoles.	8
2.1	Flux tubes penetrating a superconducting slab.	10
2.2	Critical surface of NbTi superconductor.	11
2.3	Field ramp cycle for the critical state model.	14
2.4	Current layer in Wilson Model.	15
2.5	Two arbitrarily intersecting circles.	16
2.6	Nested intersecting circles with five layers and a fixed shift c	17
2.7	Calculation of a sc. filament with the intersecting ellipse model ($N = 4$).	18
2.8	Calculation of a sc. filament with the intersecting ellipse model ($N = 10$).	19
2.9	Field ramp cycle for the intersecting ellipse model.	21
2.10	Multipoles and corresponding current distribution of the B_i	23
2.11	Geometric field error - analytic approach.	24
2.12	Multipole b_3 simulated without persistent currents.	26
2.13	Simulation of the multipole b_3 with and without persistent currents.	26
2.14	ROXIE simulation results of an LHC main bending magnet.	29
2.15	Test station for superconductor magnetization.	31
2.16	Principle of magnetization measurement.	32
2.17	Results of magnetization measurement for strands for the inner cable 01E.	33
2.18	Superconductor magnetization of the upper branch for all manufacturers.	34
2.19	Test stand for cold measurement with two dipole magnets (blue).	35
2.20	Principle of cold measurement shafts.	36
2.21	Current ramp cycle for cold magnet measurements.	37
3.1	Dependency of the upper critical flux density B_{c2} on temperature.	39
3.2	Unspecific magnetization compared to some cable measurements.	41
3.3	Multipoles resulting from the approach with the unspecific fit function.	42
3.4	Multipole b_3 resulting from the approach with the unspecific fit function.	43
3.5	Influence of fit parameter α on the scaling power law.	44

3.6	Influence of fit parameter β on the scaling power law.	44
3.7	Influence of fit parameter $C0$ on the scaling power law.	45
3.8	Functions for the unspecific fit for all cables.	47
3.9	Matching of adapted scaling power law fit with measurement data.	49
3.10	Simulated multipole b_3 for the adapted scaling power law.	50
3.11	Simulated multipole b_3 for the scaling power law with fixed ending.	52
3.12	Local magnetic induction in the coil cross section.	53
3.13	Simulated multipole b_3 for the scaling power law without pinch off.	55
3.14	The double bending function shown in different steps of development.	57
3.15	Matching of the double bending function fit with measurement data.	59
3.16	Simulated multipole b_3 for the double bending approach.	60
4.1	All fit functions used within this thesis adapted for the inner cable 01B.	61
A.1	Geometry of two intersecting circles.	66
A.2	Field of two intersecting cylinders.	67

1 Introduction

1.1 Aim of the Work

In superconducting accelerator magnets field errors are mainly created by the positioning of the conductors but also by so-called persistent currents. These currents are an inevitable property of superconducting materials and result from the fact that always the maximum current density, the so-called critical current density, is induced [1]. This creates an additional magnetic field and therefore adds a perturbation to the source field. It has been observed that cables of different manufacturers show a different superconductor magnetization behaviour which is linked to the persistent currents.

All magnets for the LHC are produced by industry and have to undergo a quality control at CERN. Therefore the field errors are measured and compared with simulations such that assembly errors e.g. illpositioning of conductors can be traced. Up to now for the simulation of field errors of persistent currents no difference between the cables of different manufacturers is made and so field errors could not be linked to the cable properties.

In general, cables are represented by their geometric properties and their function of critical current density. For this thesis, a suitable function to describe all LHC cables is to be found and the parameters are to be determined by means of fitting the available magnetization measurement data.

1.2 Outline of this Thesis

Starting from a basic introduction of the LHC (Large Hadron Collider) [12] project at CERN, those parts of superconducting magnets that are relevant for the calculation of superconductor magnetization and the theoretical background of superconductivity are explained. A fit function for the critical current density is developed and simulations with this fit function applied are carried out. The results are compared with measurements taken at cold and discussed.

Introduction

The first chapter explains briefly the LHC project and motivates the need of superconducting magnets. The basic layout of the LHC main bending magnets is shown and the most important parts with respect to magnetic field calculations, like the iron yoke, the coil cross section and the superconducting cables are pointed out. The constituent parts of the cables are described and the basic data is given.

Basics

Chapter 2 provides the necessary information in order to understand how field errors in the LHC magnets can be calculated from the layout of the magnet and the measured superconductor magnetization of the used strands.

The concepts of superconductivity are introduced. The limits of the superconducting state are shown and the persistent currents and the hysteresis effect for hard superconductors are explained. Three models for superconductors are introduced: the critical state model [1], the Wilson model [21] and finally the intersecting ellipse model that has been used for the calculation of the field errors in this thesis.

The quality of the field in the aperture of the LHC main dipole magnets is expressed by means of a multipole expansion. For a simplified geometry the influence of symmetries of the created harmonic field errors is investigated for the excitation currents and for the persistent currents due to superconductor magnetization.

The principles of the magnet simulation are explained and the CERN field computation program ROXIE is introduced. The influence of the different parts of the magnet on the field in the apertures can be seen from the steps of field computation like the calculation of the coil field, the field of the iron yoke and the field of the persistent currents.

Since the critical current density is in general not directly accessible it is obtained by means of a superconductor magnetization measurement. The measurement principles are explained and the connection between magnetization and critical current density is shown.

Fit Function for the Critical Current Density

In chapter 3 the multiple dependencies on the critical current density are shown and the scope is set on the dependency on the applied magnetic induction. The temperature dependency is taken from other approaches.

In a first approach the scaling power law given by Bottura is adapted. The so obtained critical current fit shows only very small critical currents for high applied fields which causes a smaller hysteresis width for high excitation currents. All variations of this approach can not take care of this missing feature. Furthermore it is shown that this approach shows an unphysical behavior for its given parameter range.

A new function which can easily be adjusted to the measurement data is introduced and gives a very good fit of the magnetization data.

1.3 The Large Hadron Collider

At CERN¹ the Large Hadron Collider (LHC) [12] is currently under construction. The LHC is a superconducting particle accelerator that will provide proton-proton collisions, as well as collisions of lead ions. The aim of this collider is not only to produce a higher collision energy, but also a higher luminosity² than that of already existing hadron colliders.

¹Organisation Européen pour la Recherche Nucléaire

²The rate of interaction per unit cross-section.

In order to recreate the conditions which existed in the universe just 10^{-12} seconds after the "Big Bang", LHC will provide proton-proton collisions with a center-of-mass energy of 14 TeV and a luminosity of $10^{34} \text{ cm}^{-2}\text{s}^{-1}$. It will also provide heavy (Pb) ion collisions with a center-of-mass energy of more than 1000 TeV and a luminosity in excess of $10^{27} \text{ cm}^{-2}\text{s}^{-1}$.

The LHC ring of approximately 27 km of circumference consists of 1232 dipole magnets to bend the particles, 308 quadrupole magnets to focus the beam and a large number of higher multipole corrector magnets. At 4 points one of the big experiments CMS, ATLAS, ALICE and LHC-B are inserted.

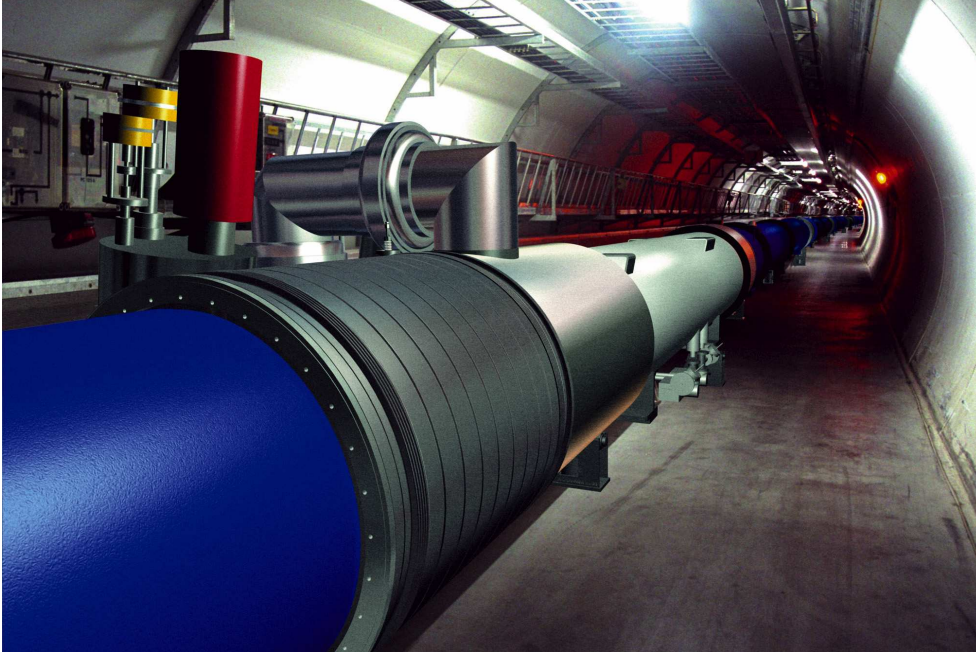


Figure 1.1: Computer graphic of the LHC tunnel after completion with dipole magnets (blue) and quadrupole magnets (white).

During operation the beam will be injected from the pre-accelerator chain using all other accelerators at CERN with a low injection energy and then accelerated up to the nominal energy for the experiments. Therefore the magnetic induction is synchronously ramped up from the injection field of 0.57 T (corresponding to an excitation current of 760 A) to the nominal field of 8.5 T (11800 A).

1.4 Superconducting Magnets

In order to reduce the cost of civil engineering, the existing LEP³ tunnel is used for the new accelerator. Since the mass of protons or even lead ions is much higher than the mass of an electron a stronger Lorentz force is needed to bend a particle beam of same

³Large Electron Positron Collider - decommissioned in November 2000.

velocity on a circular trajectory with a fixed radius. Normal conducting magnets are limited to maximum magnetic inductions of up to 2 T [20, p. 68] and cause due to the electrical resistivity huge power consumption and heating. These two arguments lead to superconducting magnets with field strengths up to 9 T.

1.4.1 LHC Main Bending Magnets

In order to bend the proton beam on its circular trajectory a very strong magnetic induction of high homogeneity is needed. Every deviation in the dipole field causes an additional force on the particle which makes the beam leaving the optimal trajectory. The deviation of the beam position has to be corrected by small corrector magnets in order not to lose the beam and to guaranty a high beam luminosity. Theoretically a perfect homogeneous dipole field can be obtained inside a cylinder of infinite length with $\cos \theta$ depending surface currents. In the same way the perfect field of the so-called higher order multipoles can be obtained with a $\cos n\theta$ current distribution.

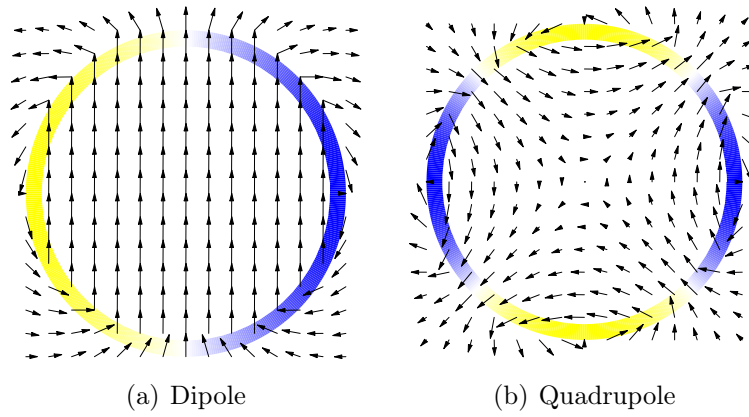


Figure 1.2: Ideal current distribution and field of magnetic induction.

For the LHC main dipole magnets the ideal $\cos \theta$ current distribution is practically approximated by putting the conductors in two layers around the beam pipe. The approximation is limited by the size and the shape of the used cables and thus always causes field errors. The space between the cables which is not needed for a conductor is filled with non-magnetic copper wedges. By reshaping the copper wedges the layout of the so-called coil cross section was twice varied during the production process in order to change the conductor position and so to improve the characteristic field error. The different cross sections are denoted by the numbers 1 to 3. Table 1.1 shows the number of magnets produced with each cross section layout.

Table 1.1: Number of magnets produced with each cross section layout until end of 2004.

Coil cross section	Number of Magnets
1	27
2	146
3	455

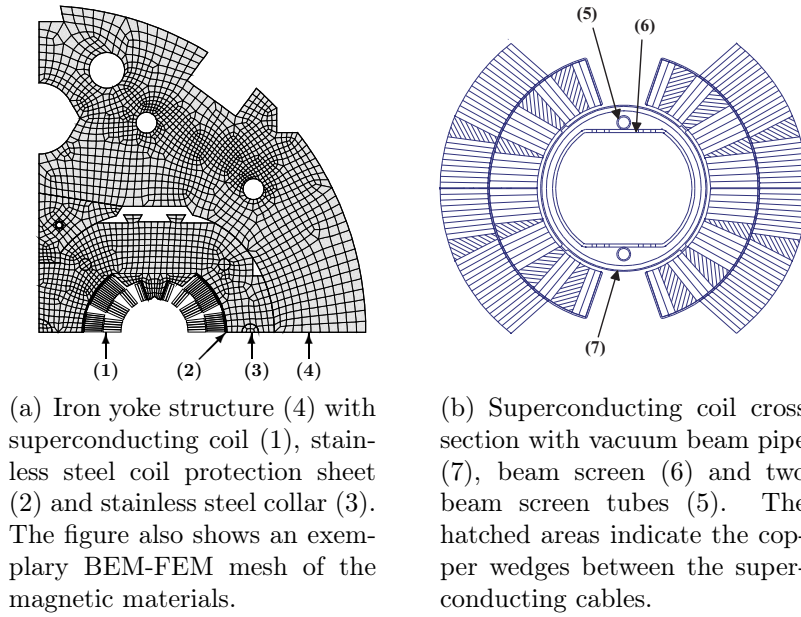


Figure 1.3: Cross section of the LHC main dipole magnet (Pictures with the courtesy of C. Völlinger).

The superconducting coil is covered by a so-called coil protection sheet made of stainless steel and put under pressure into a collar of laminated stainless steel in order to keep the coil in place under the influence of the enormous Lorentz forces. The collar shall prevent any conductor movement during operation due to Lorentz forces. If a conductor moves the friction produces enough heat to cause a quench (unwanted transition from superconducting to normal conducting state) and the field characteristic changes due to the new conductor position.

Proton-proton colliders require two separate beam channels with fields that are equal in strength but opposite in orientations in order to bend particles that have identical electrical charges. Due to the limited space in the already existing LEP tunnel, a so-called two-in-one design was chosen for the LHC dipoles where the two beam channels are incorporated into a common collar structure and one single yoke (see fig 1.3 a)). This causes an additional field error due to cross-talk effects between the two apertures.

The collared coil is surrounded by a laminated iron yoke in order to close the flux lines and to concentrate the magnetic flux density in the apertures. The yoke yields $\approx 18\%$

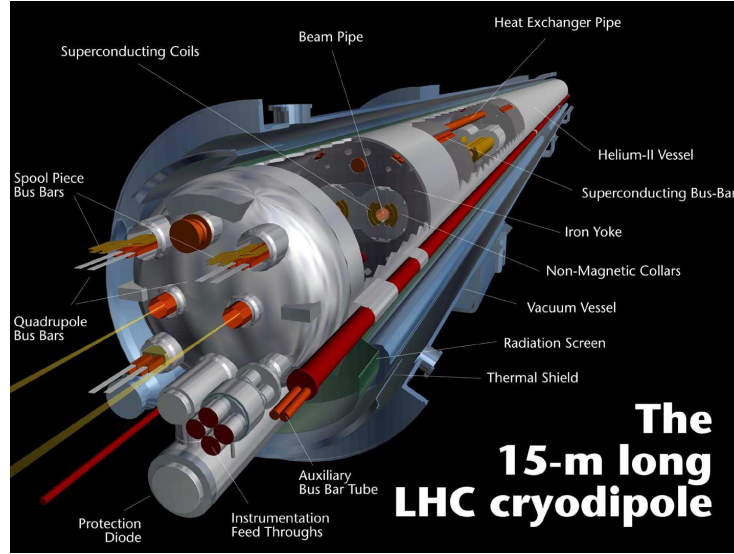


Figure 1.4: Exploded view of an LHC main dipole (©CERN).

additional field strength. Furthermore the iron shows a saturation effect for high currents and additional field errors resulting from the yoke are produced.

The whole construction is welded into a shell of steel which also provides the helium-vessel and builds the so-called cold mass. The cold mass is flooded during operation with super fluid helium at a temperature of 1.9 K. The magnet is put into a cryo-vessel and is completed by super insulation bridging the temperature difference of approximately 300 K and the connections for helium and current.

Figure 1.4 shows a picture of the dipole with the most important parts highlighted. In fig. 1.5, a sketch of all described parts is shown.

1.4.2 Cable for the LHC Main Dipole Magnets

The coils of the LHC main dipole magnets are built of superconducting Rutherford type cables. In order to obtain a $\cos\theta$ current distribution these cables are pressed into a trapezoidal shape, the so-called keystoneing which has the side effect of causing a gradient in current density across the coil cross section towards the center. Because of the higher magnetic field in the inner regions of the coil, different cables are used for inner and outer layer. They differ in number of strands, critical current values and geometrical dimensions. In tab. 1.2 the basic data of the used cables is given [5].

LHC DIPOLE : STANDARD CROSS-SECTION

CERN AC/DI/MM - HE107 - 30 04 1999

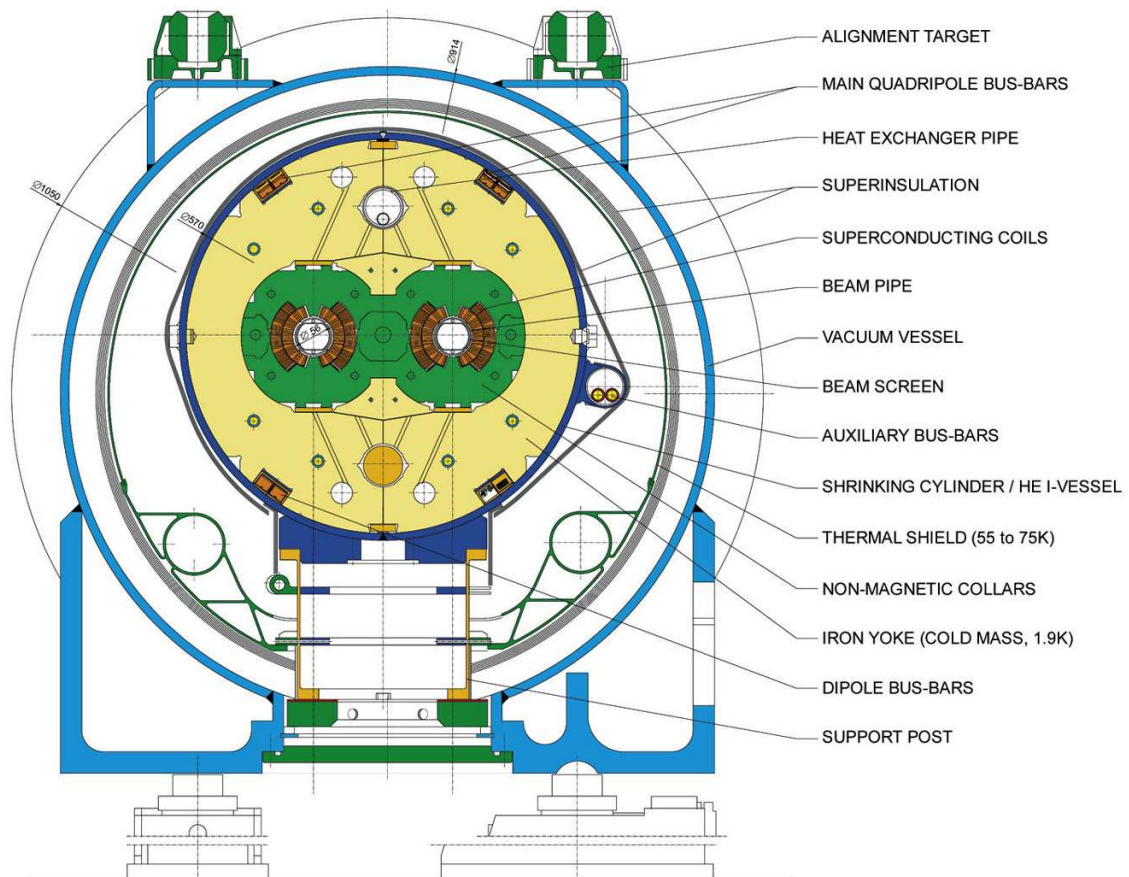


Figure 1.5: Sketch of the an LHC main dipole (©CERN).

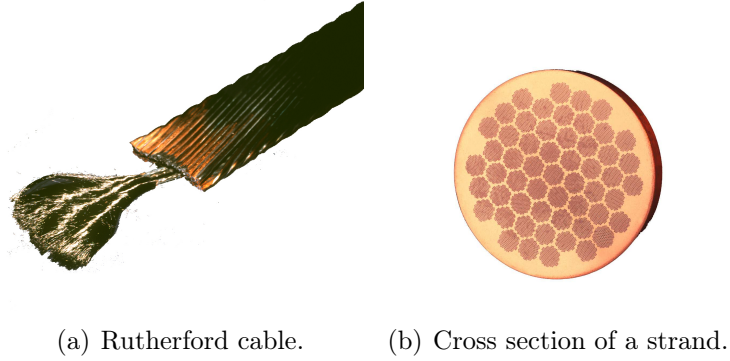


Figure 1.6: Cable for LHC main dipoles (©CERN).

Each strand consists of superconducting NbTi filaments embedded in a copper matrix with different number of filaments for inner and outer layer, as well as different filament diameter. Also the strand diameter and the superconductor to copper ration (Cu:Sc) differs for inner and outer layer.

Table 1.2: LHC Cable Data.

Parameter	Inner Cable	Outer Cable	Unit
Number of Strands	28	36	
Strand Diameter	1.065	0.825	mm
Filament Diameter	7	6	μm
Number of Filaments	8900	6500	
Cu:Sc Ratio	1.65	1.95	(by volume)
Reference value for critical current density $J_{c,ref}$ at 5 T and 4.2 K	3	3	kA/mm^2

The whole cable production is shared by six firms where the firms denoted by the letters B and E produce the inner cables denoted by 01 and the companies denoted by the letters B, C, D, G and K produce the outer cables denoted by 02. This gives theoretically the total number of ten combinations however, some are omitted. Table 1.3 shows the number of magnets produced with a certain cable combination up to end of 2004.

Table 1.3: Number of magnets produced with each cable combination.

	02B	02C	02D	02G	02K
01B	222	4	-	138	173
01E	26	-	-	52	13

2 Basics

2.1 Superconductivity

In 1911 K. ONNES discovered that some materials lose all electrical resistivity if cooled down below a certain temperature [14]. When this so-called critical temperature T_c is reached a sudden jump of resistivity from finite values to values very close to zero ($\approx 10^{-15} \Omega$) can be observed. This phenomenon is denoted as superconductivity.

The critical temperature is an intrinsic property of the material determined mainly by the chemical composition and crystal structure [19],[9]. In alloy materials it is relatively unaffected by metallurgical treatments like the process of drawing the strands or winding the cables. For this reasons the critical temperature can be considered as constant in this thesis for all cables used for the LHC main dipole magnets.

The superconducting state is also limited by the magnetic induction (applied to the superconductor). According to the reaction on an applied magnetic field two types of superconductors can be differentiated.

The so-called **Type I superconductor** totally expels an external field up to an upper critical value B_c . For higher values of magnetic induction it transits to the normal conducting state. Type I superconductor are mostly metallic materials e.g. lead and niobium.

The expulsion of the external magnetic induction is done by surface currents which create an internal field cancelling out the external field. This screening effect was discovered by MEISSNER and OCHSENFELD and they showed that the screening currents are always induced independent whether the field changes or the superconductor is cooled down in a constant field [14]. These induced currents differ from known eddy currents such that they do not decay with time and they are macroscopically equal to ideal diamagnetic magnetization currents [19].

For Type I superconductor the screening currents can be described by the LONDON equations. If a superconducting slab is exposed to a magnetic induction the screening effect leads to an exponential decay of the applied induction to zero within the London penetration depth and is defining the Meissner phase [19, p. 14].

Superconductors of Type I are not practical for the construction of accelerator magnets because they can not guide currents of a technically interesting magnitude. All currents create a magnetic field which is expelled from the inner of the superconductor and so the current distribution is limited to the surface area where the magnetic field and the current density coexist. The additional magnetic induction of the transport current decreases the screening ability for external fields [19].

The second type - the so-called **Type II superconductor** - expels an external magnetic

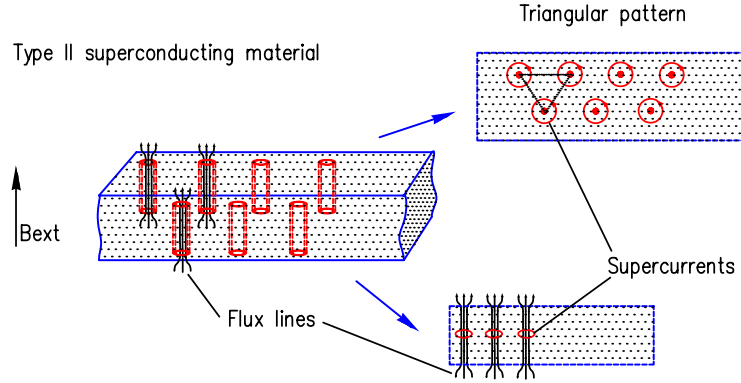


Figure 2.1: Flux tubes penetrating a superconducting slab. They are built by so-called supercurrents and arrange in triangular patterns.

induction first up to an upper critical value B_{c1} similar to the Type I superconductor. However, for higher values, the magnetic flux penetrates the superconductor in so-called flux tubes (illustrated in fig. 2.1). In this way the superconductor can be exposed to much higher values of magnetic induction up to the second upper critical value B_{c2} . For values higher than B_{c2} the superconductor transits to normal conducting state. Typical Type II superconducting materials are e.g. NbTi and Nb₃Sn.

Every flux tube is built by so-called supercurrents and carries always the same quantised amount of magnetic flux [6]. They are guiding the flux through the superconductor in little bunches. Due to the supercurrents they are interacting with each other and so without any transport currents they arrange themselves in a triangular mesh. Every change of the external field causes a change in the number of flux tubes and then a movement of flux tubes takes place in order to rearrange. These movements create heat and thus can cause an unwanted loss of superconductivity. Such an unwanted loss of superconductivity is called a **quench**.

Since transport currents cause even more movement of flux tubes due to the Lorentz forces superconductor of Type II are also limited in their capability to carry currents. In **Hard Superconductors** small impurities so-called pinning centers are inserted into the superconducting material in order to limit the freedom of movement of the flux tubes. The pinning centers capture flux tubes and prevent them from moving. Due to the interaction of the flux tubes with each other all flux tube movement is reduced in the specimen.

Raising the external magnetic induction after cooling down a hard superconductor to the superconducting state yields an increasing number of flux tubes depending on the amount of flux. When the field is reduced again, the flux tubes can not arrange themselves according to the external flux because a lot of them are pinned and can not move freely. Additional flux tubes of opposite orientation are induced and thus cause a hysteresis on the overall measured superconductor magnetization and are the source of a hysteresis loss. Since the induced superconductor magnetization currents remain after reducing the external field again to zero and since they do not decay with time they are called **persistent currents**¹.

¹The superconductor magnetization currents in type I and type II superconductors do not decay with

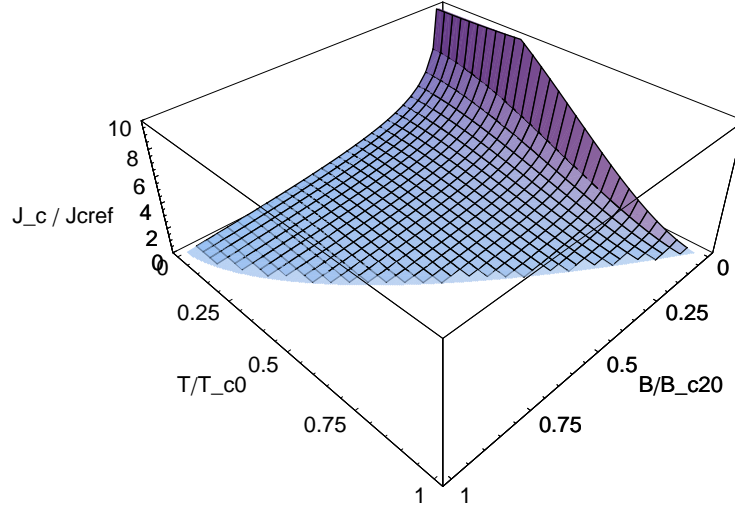


Figure 2.2: Critical surface of NbTi superconductor.

With pinning centers transport currents can be guided without creation of heat production.

With these modification hard superconductors can be used for the construction of accelerator magnets with very high values of magnetic induction and very high currents. As a side effect superconductivity comes with persistent currents influencing the current distribution and the pinning comes with a hysteresis of magnetization.

In addition to the critical temperature T_c and the upper critical field B_{c2} , the superconducting state is limited by the critical current density J_c . The critical current density is depending on the applied magnetic induction and the local temperature. Exceeding the critical current density also causes a quench.

Figure 2.2 shows the limits of the superconducting state for an exemplary cable. The surface shown is called 'critical surface' of a superconductor and separates the superconducting from the normal conducting phase. All states below this surface are superconducting.

2.2 Model of a Hard Superconductor

For the computation of large accelerator magnets the basic ideas of hard superconductors shown in section 2.1 are not useful. To the author's knowledge it is not possible to describe flux tubes with Maxwell's theory without considering quantum effects. A description of flux tubes necessitates the calculation of every filament in the superconductor in a three dimensional model because the flux tube distribution depends on the local field and is discrete. The difference of many magnitudes in size of the flux tubes and the aperture or

time too, but they depend on an external field. To the authors knowledge the term *perisistent currents* is only used for hard superconductors.

the magnet presents a problem of currently unsolvable complexity.

For these reasons a theory based on Maxwell's law is needed which describes in a good approximation the macroscopical effects of magnetization of hard superconductor like the hysteresis and the influence on the current distribution.

2.2.1 Critical State Model

The critical state model was developed by C. P. Bean in 1964 for a slab of hard superconducting material [1] and shall be shown here because of the simple geometric dependences.

As mentioned in section 2.1 the superconducting state is limited by the critical current density. The basic premise of the critical state model is that any magnetic field, however small, **always induces the maximum critical current density** in the superconductor in order to screen the inner of the superconductor. Furthermore, for the model the dependency of the current density on the applied magnetic induction, on the local magnetic induction in the slab and the Meissner phase are neglected. Therefore the current density in the superconductor is either zero in field free regions or of constant value $\pm J_c$.

In the following a superconducting slab parallel to the yz -plane of infinite length and thickness D is considered. The origin shall be located in the middle of the slab. When this slab is exposed without limitations to an tangential y -directed magnetic field, a screening current density in z -direction is induced according to the right hands law.

In a first thought it can be assumed that for small values of the applied magnetic induction the inner field decays to zero within a certain length d with $d \leq D/2$. This length is called penetration depth and thus the critical current density becomes a step function of the position and the penetration depth.

$$J(x) = J_c (1 - \Pi_{2(D/2-d)}(x)) \operatorname{sgn}(x).$$

Here $\operatorname{sgn}(x)$ denotes the so-called signum function and $\Pi_{2(D/2-d)}(x)$ denotes a centered unit step which takes the value 1 for $x = -D/2 + d$ up to $x = D/2 - d$ and equals zero for the rest.

The static Maxwell's equation $\vec{\nabla} \times \vec{H} = \vec{J}$ yields for an one dimensional problem

$$\frac{\partial H_y}{\partial x} = J_z$$

where H_y denotes the local magnetic field and J_z the constant current density J_c . With the linear material equation of empty space $B = \mu_0 H$ the local dependency of the inner magnetic induction B can be obtained by integration.

$$B = \mu_0 J_c (|x| - D/2 + d) (1 - \Pi_{2(D/2-d)}(x)) + B_0. \quad (2.1)$$

Since the tangential magnetic field has to fulfill the continuous boundary condition and the permeability of empty space is considered, Eq. (2.1) has to meet the applied magnetic induction for $x = \pm D/2$. With increasing applied magnetic induction the penetration depth increases until the slab is completely penetrated. Then the inner field rises uniformly

with the external field by increasing the constant B_0 . In this way the field and current distribution can be approximated up to the upper critical field B_{c2} .

From a certain state of applied external magnetic induction a decrease of field strength is modeled by superposing a field with opposite orientation. This, however small, superposed field induces a current layer of opposite direction and so adds an opposing linear term to the equation. The solution still has to meet the external field. In this way a new current layer is created and the magnetic induction is changed from the outer to the inner part of the slab. Each time when the field increases or decreases an additional current layer with opposite polarity is produced and grows from $x = D/2$ into the interior of the slab (except the wipe-out-condition is reached).

The constant B_0 varies only when the field of full penetration is exceeded and the condition of meeting the external field can not be fulfilled by the linear terms.

Figure 2.3 shows the inner magnetic induction and current density of a slab for a ramp cycle of the external magnetic induction from zero to a state above full penetrated state and down to zero field.

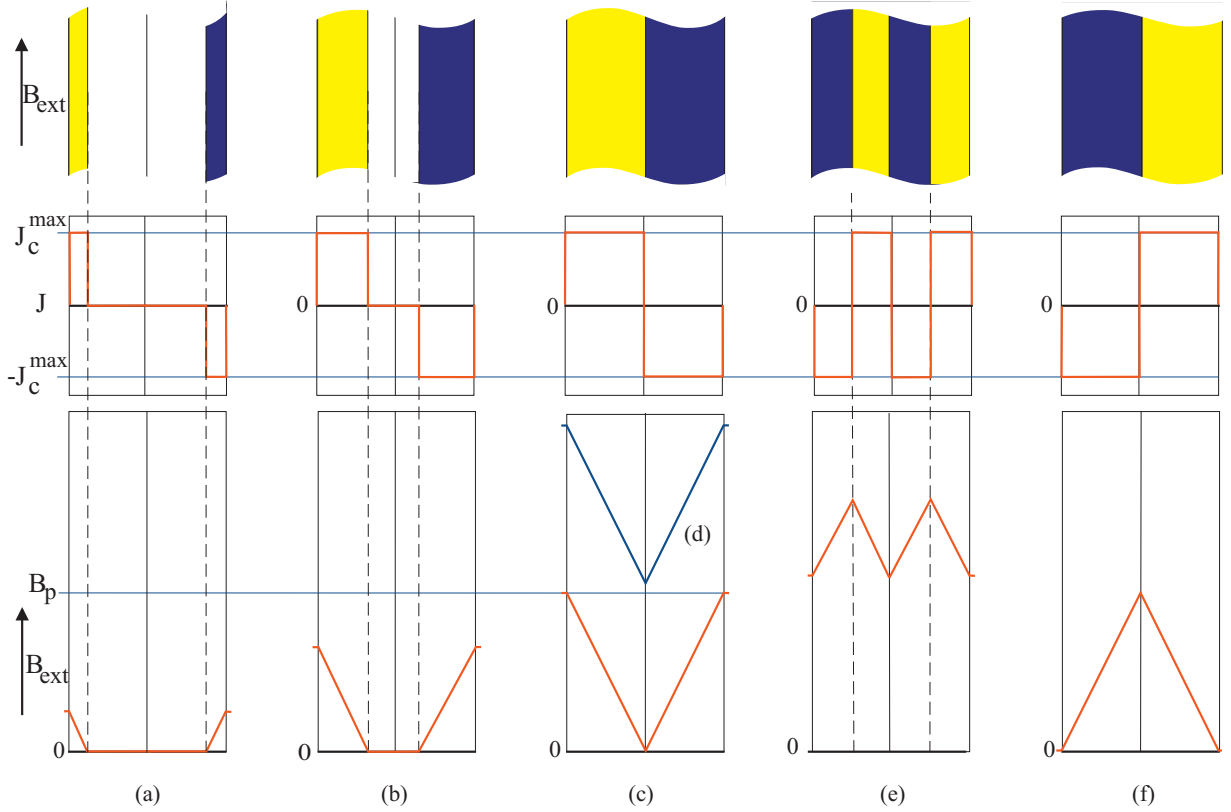


Figure 2.3: Field ramp cycle for the critical state model (Picture with the courtesy of C. Völlinger).

- (a),(b)** The external field is ramped up. The internal field decreases linearly within the length $D/2$ and the superconductor is not fully penetrated. The equation (2.1) can be solved without the constant B_0 .
- (c)** The field reaches the level of full penetration and $d = D/2$. The only point of zero field is in the center of the slab.
- (d)** The field is increased further and the equation (2.1) now yields a constant B_0 bigger than zero.
- (e)** The external field is decreased again. A new opposing layer of current density is created. The distribution of magnetic induction is now given by the two linear terms and the constant B_0 which has yet not been affected by the change of external field.
- (f)** The external field is zero. The opposing current density fully penetrates the slab. The magnetic induction is given by the second linear term and the constant which still remains and thus creates the hysteresis of the magnetization.

2.2.2 The Wilson Model

Applying the ideas of Bean to a superconductor of infinite length and circular cross section and considering the critical current density to be a function of the external field leads to the Wilson model² as presented in [19, p. 33ff].

In order to screen the inner part of a cylinder in a homogeneous perpendicular field a current distribution is needed which creates an opposing field cancelling out the external field. In the Wilson model the screening current is located in layers between the circular material border and an inner ellipse of varying ellipticity which becomes a line for fully penetrated state. This does not create a perfect homogeneous field in the inner current free region but is considered as sufficiently precise for the model.

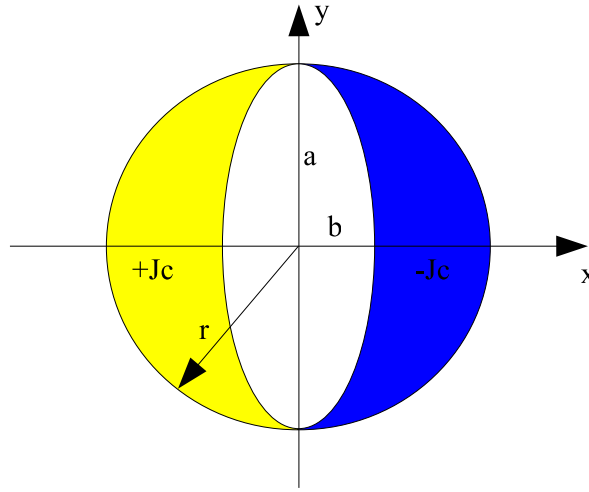


Figure 2.4: Current layer in Wilson Model.

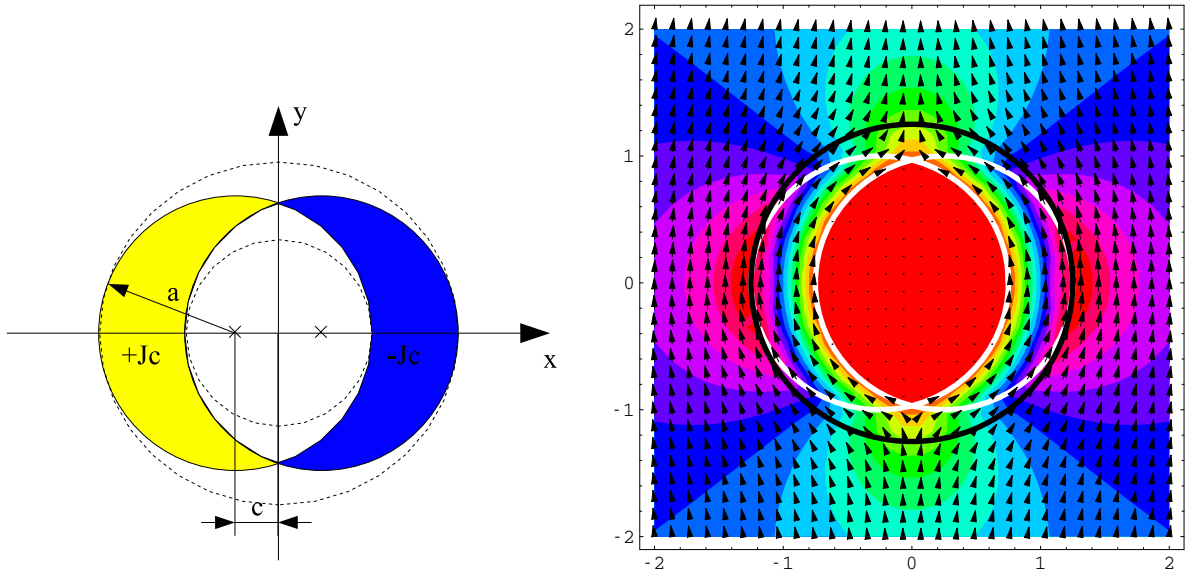
In the same way like in the critical state model layers of constant current density are created in order to match the changes of the external field. The current density itself depends now on the external magnetic induction. With a critical current density that strongly increases with decreasing applied magnetic induction this modification yields a more pronounced screening effect for small fields than in section 2.2.1 and larger regions within the filaments cross section stay field free.

2.2.3 The Intersecting Ellipse Model

The intersecting ellipse model of Völlinger [19] was also developed for a superconducting filament but provides in addition to the Wilson model a local field dependency of the critical current density. The main idea is based on the homogeneous field of two intersecting circular cylinders.

²The dependency of the critical current density on the applied external magnetic induction is not mentioned in [21], but the used formulae allow this modification without any restrictions

As shown in appendix A two intersecting cylinders shifted out of the origin by the amount c and carrying a constant current density J_c produce a homogeneous field $B_y = -\mu J_c c$ in the overlapping area. Superimposing an external homogeneous field of magnetic induction parallel to the y-axis to the field of the two intersecting cylinders (as shown in fig. 2.5 a)) yields a current free region in the center of the filament with a reduced homogeneous field $B = B_{ext} - \mu J_c c$. Figure 2.5 b) shows the screening effect for an external field of equal but opposite strength to the internal field ($B_{ext} - \mu J_c c = 0$) of the intersecting cylinders. The eye shaped area in the center (red) is of zero field and current density.



(a) Geometry - c denotes the grade of intersection and the shift of both circles out of the origin. The radius of the intersecting circles is given by a . The dashed circles show the reference radius for the nesting of several intersecting circles.

(b) Field distribution of the geometry shown left with an applied external field perpendicular to the filament and parallel to the y-axis. The color indicates the modulus of the magnetic induction. The eye-shaped area in the center stays field free.

Figure 2.5: Two arbitrarily intersecting circles of oppositely oriented constant current densities.

In order to model superconducting filaments by using the basic idea of intersecting circles in a first step the current density is connected to the magnetic induction outside the cylinder at the point $(x = a + c, y = 0)$. For the screening of an external field only the parameter c can be changed and has to be increased for an increasing field. With increasing shift c the field free eye shaped area decreases and so the screening effect for the filament is reduced.

The screening can be improved by nesting a series of intersecting circles. Therefore each new layer is placed into the inner circle of the previous layer. The current density is chosen from the **local** magnetic induction at the outer crossing of the circle with the x-axis as before. Due to the observed inverse proportionality between the critical current density

and the local magnetic induction the current density increases from layer to layer since the external field is more and more screened. The overall screening effect increases with the number of layers created.

As shown in [19, p. 48f] for a constant shift $c = R/(2N)$ with R the filament's radius and N the number of layers, the filament can be filled completely ending up with two touching circles of radius $a_N = c$. For this pattern the radii a_i are given by:

$$a_i = R \frac{2N - 2i + 1}{2N}.$$

Using the term for expressing the magnetic induction B_\odot of a cylindrical current distribution J_c of radius a

$$\vec{B}_\odot(\vec{r}, a, J_c) = \frac{\mu_0 J_c a}{2} \vec{e}_\phi \begin{cases} \rho/a & \rho \leq a \\ a/\rho & \rho > a \end{cases}$$

the local magnetic field for N layers is given by the following recurrent equations:

$$B(i) = \begin{cases} B_{ext} & i \leq 1 \\ B(i-1) - \mu J_c (B(i-1))c & i > 1 \end{cases}. \quad (2.2)$$

$$\vec{B}(\vec{r}) = \sum_{i=1}^N \pm \vec{B}_\odot(\vec{r} \pm c \cdot \vec{e}_x, a_i, J_c(B(i))). \quad (2.3)$$

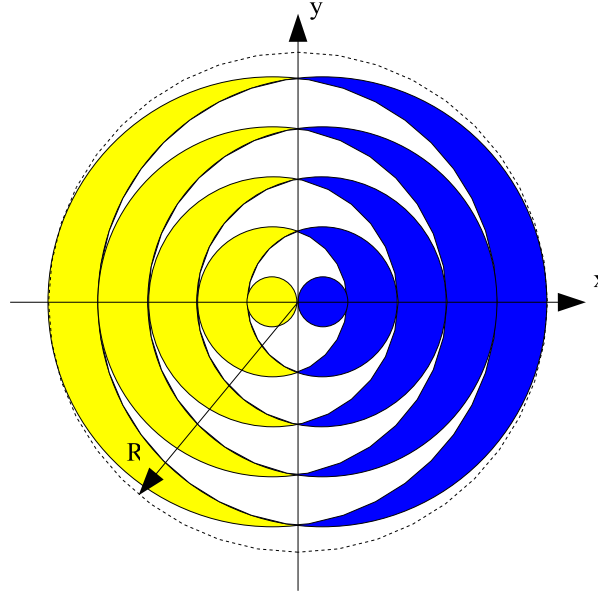
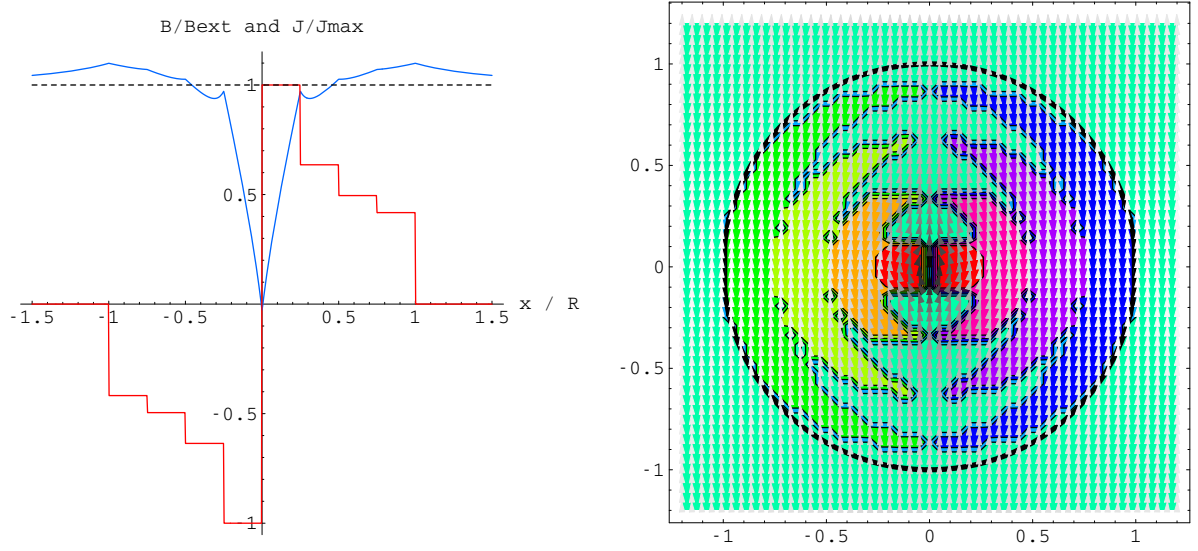


Figure 2.6: Nested intersecting circle with five layers and a fixed shift c . The last layer is built by two touching circles.

In Figure 2.7 the field and current distribution for an exemplary filament calculated from Eqs. (2.2) and (2.2) is shown. The number of layers is set to $N = 4$. A similar

geometry with $N = 5$ is shown in fig. 2.6. It can be seen that the magnetic induction decreases towards the center of the filament but stays larger than zero. For the current density the first steps are of approximately the same amount, but towards the center J_c increases strongly. This is to be expected from the critical current density dependency on the applied magnetic induction shown in fig. 2.2.



(a) Normalized current (red) and field (blue) distribution along the x- axis.

(b) Local current (shading) and field (arrows) distribution.

Figure 2.7: Calculation of a superconducting filament exposed to a perpendicular magnetic induction with the intersecting ellipse model. The number of layers is $N = 4$ and only one iteration is done. The filament is in a fully penetrated state.

Although the field plot in fig. 2.7 seems to be homogeneous across the filaments cross section it varies in strength and direction. A current distribution like two intersecting circles only produces a homogeneous field in the center area. For this reason all nested pairs change the field in the outer layers.

For fig. 2.8 the number of layers is $N = 10$ and the same external field is applied. The current density of the first 4 layers is rather small and does not have a big effect on the external field. The current in the 5th layer (always counted from outside) is according to the already screened field rather big and decreases the local field within one step to zero. The magnetic flux is pushed out of the filament's center and thus creates an additional field around the 5th current layer and the superconductor. It should be noticed that with an increasing number of layers, the screening effect is improved and the field distribution becomes smoother.

With a fixed shift c for all layers a not fully penetrated filament is not easily described because the last current layer before the field free region either does not cancel the center field or overdoes and creates a negative central field. The screening capacity is determined

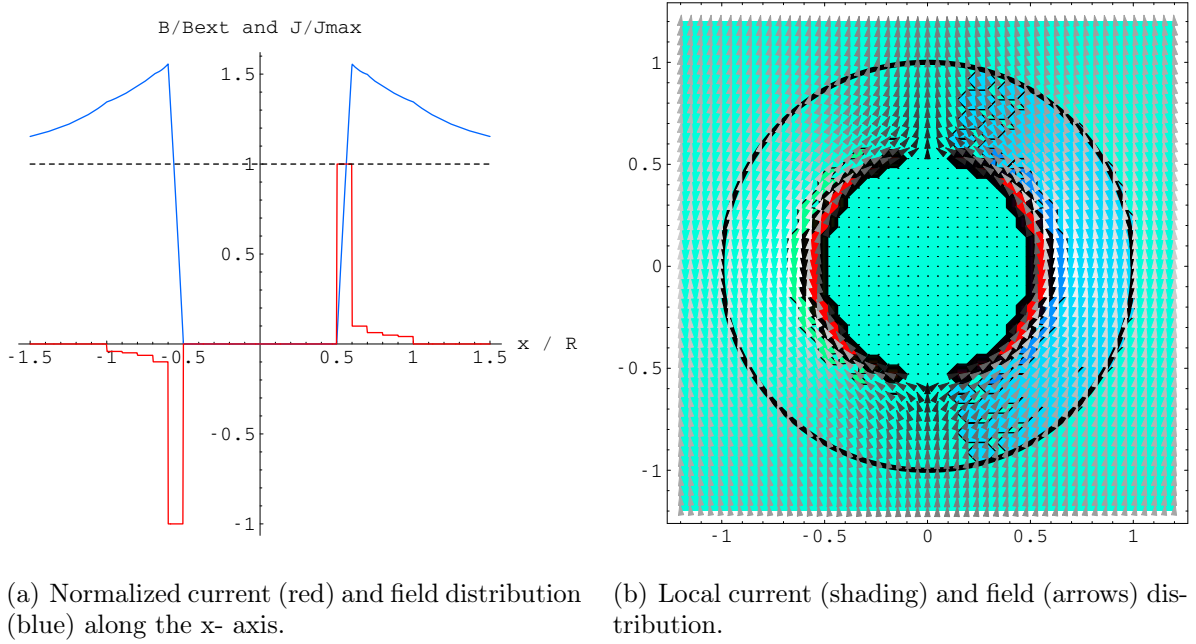


Figure 2.8: Calculation of a superconducting filament exposed to a perpendicular magnetic induction with the intersecting ellipse model. The number of layers is $N = 10$ and only one iteration is done. Compared to the calculation shown before, the value of the applied magnetic induction was not changed, but the increased number of layers yields a not fully penetrated filament. I.e., the inner part of the filament stays current and field free.

by c and $J_c(B_{local})$ and so in general it can not end up with zero field. The last layer then has to be of free shift c .

By evaluating the limit for an infinite number of layers with infinitesimal thickness the discrete sum in Eq. (2.3) yields an integral and gives a continuous function for the local magnetic induction and the current density. For a not fully penetrated filament magnetic induction and the current density decrease to zero towards the center and define the so-called penetration depth.

Like in the models of Bean and Wilson the current distribution is used in a hysteresis model. Therefore the current distribution according to an applied magnetic induction is superimposed to the current distribution of the changing field. This yields one current layer³ for each field change. In fig. 2.9 an analogous field ramp cycle as introduced in section 2.2.1 is shown.

As already shown the nested intersecting circles create an increase of the local magnetic field at the boundary of the filament. As a consequence, the obtained value for the current density of the first layer does not match to the resulting local field. With the new external

³After the evaluation of the limit for an infinite number of layers the distribution is continuous. Then layers are only created by field changes and therefore stay discrete.

field obtained from the superposition, all current layers from the outside to the inside have to be recalculated (iteration). Since the starting value was bigger then the previous field the screening for this iteration is less effective and the resulting overshoot at the filaments boundary is too small. The recalculation now is done until the value of the over shooting external field convergences.

With the nested intersecting circles a current density distribution depending on the local magnetic induction is created. Since the shape of the layers is fixed the local current distribution is only a function of magnetic field and its history. It is only indirectly depending on the considered location in the filaments cross section.

In [19] the model is also derived for intersecting ellipses. This results in a better use of the area of the cross section and thus in a better screening but is not used for the simulation program⁴ and so will not be explained.

⁴For an external field of arbitrarily changing direction only intersecting circles with the inscribed dashed circle can follow optimally

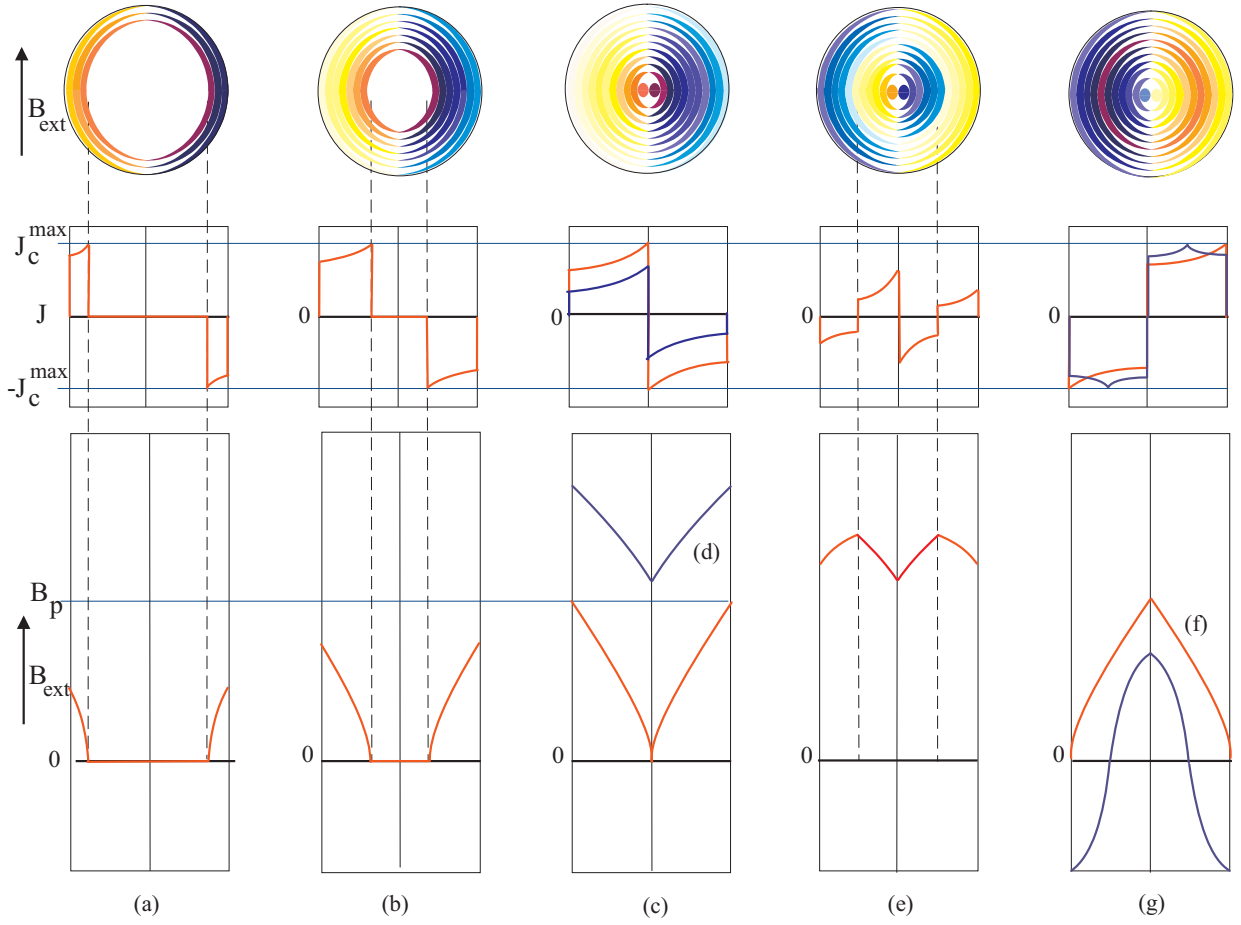


Figure 2.9: Field ramp cycle for the intersecting ellipse model (Picture with the courtesy of C. Völlinger).

- (a),(b)** The external field is ramped up. The internal field decays within the penetration depth d ($d < D/2$) and the superconductor is not fully penetrated. With increasing field the slope of the critical current density for large radii decreases.
- (c)** The field reaches the level of full penetration and $d = D/2$. The only point of zero field is in the center of the slab.
- (d)** The external field is increased further and the internal field rises according to the reduction of the screening effect due to the dependency of critical current density on the external magnetic induction. The internal field is different from zero.
- (e)** The external field is decreased again. A new opposing layer of current density is created due to the superimposed negative field. The distribution of magnetic induction is now given by the superimposition of the field of both layers and the constant offset created while raising the field above the fully penetrated state.

- (f) The external field is zero. The opposing current density fully penetrates the slab. The magnetic induction is given only given by the new opposing current layer and the constant which still remains and thus creates the hysteresis of the magnetization.

2.3 Field Errors

As mentioned in section 1.4 the field of the LHC accelerator magnets has to fulfill very strong conditions of field quality. Since the current distribution is never an exact $\cos\theta$ distribution and since due to the persistent current magnetization additional bipolar currents are induced in the filaments there is always a deviation from a perfect dipole field.

In order to set up limits for the field errors a form of the Fourier expansion is used to split the created field into equivalent ideal multipole magnets. This method can be applied either for the simulation or for the measurement results of cold magnets.

The field errors are created by the deviation of the current distribution from the ideal $\cos\theta$ shape and therefore influenced by the position of the conductor and the current they carry. With good knowledge of the geometrical effects on the field errors an inverse calculation of the conductor alignment can be performed.

Due to nonlinear iron material and the persistent currents the field error depends on the magnetic induction. Since the magnetic induction varies across the cross section of a magnet but in general increases with increasing excitation current, the multipoles are usually plotted versus applied current.

2.3.1 Multipole Expansion

For an arbitrarily field of magnetic induction in a current free region the normal field at a reference radius r_0 is considered. Since the dependency of the normal field then yields to be 2π -periodic it can be expanded by a Fourier expansion.

$$B_r(r_0, \phi) = \sum_{n=1}^{\infty} [A_n \cos(n\phi) + B_n \sin(n\phi)] \quad (2.4)$$

$$= B_N \sum_{n=1}^{\infty} [a_n \cos(n\phi) + b_n \sin(n\phi)]. \quad (2.5)$$

The A_n denote the contribution to the analyzed field of the n^{th} ideal skew multipole while the B_n denote the normal contribution. Both are a function of the used reference radius. Usually these Fourier coefficients are normalized by the main field of the analyzed structure and then given as relative values a_n for the skew and b_n for the normal component. For a dipole with vertical field B_N is given by B_1 . The a_n and b_n are usually expressed in units of 10^{-4} . The Fourier coefficient B_0 does not exist since it would not represent a field of zero divergence for the magnetic induction as postulated from Maxwell's laws!

The Fourier coefficients are calculated by:

$$A_n = \frac{1}{\pi} \int_0^{2\pi} B(r_0, \phi) \cos(n\phi) d\phi, \quad (2.6)$$

$$B_n = \frac{1}{\pi} \int_0^{2\pi} B(r_0, \phi) \sin(n\phi) d\phi. \quad (2.7)$$

In this way the field in the aperture of the LHC magnets can be split into the contribution of ideal multipole components. For the beam these have to be corrected by additional corrector magnets and therefore taken into account for the design of the machine and the construction of the magnets. For each multipole certain limits are defined which must not be exceeded.

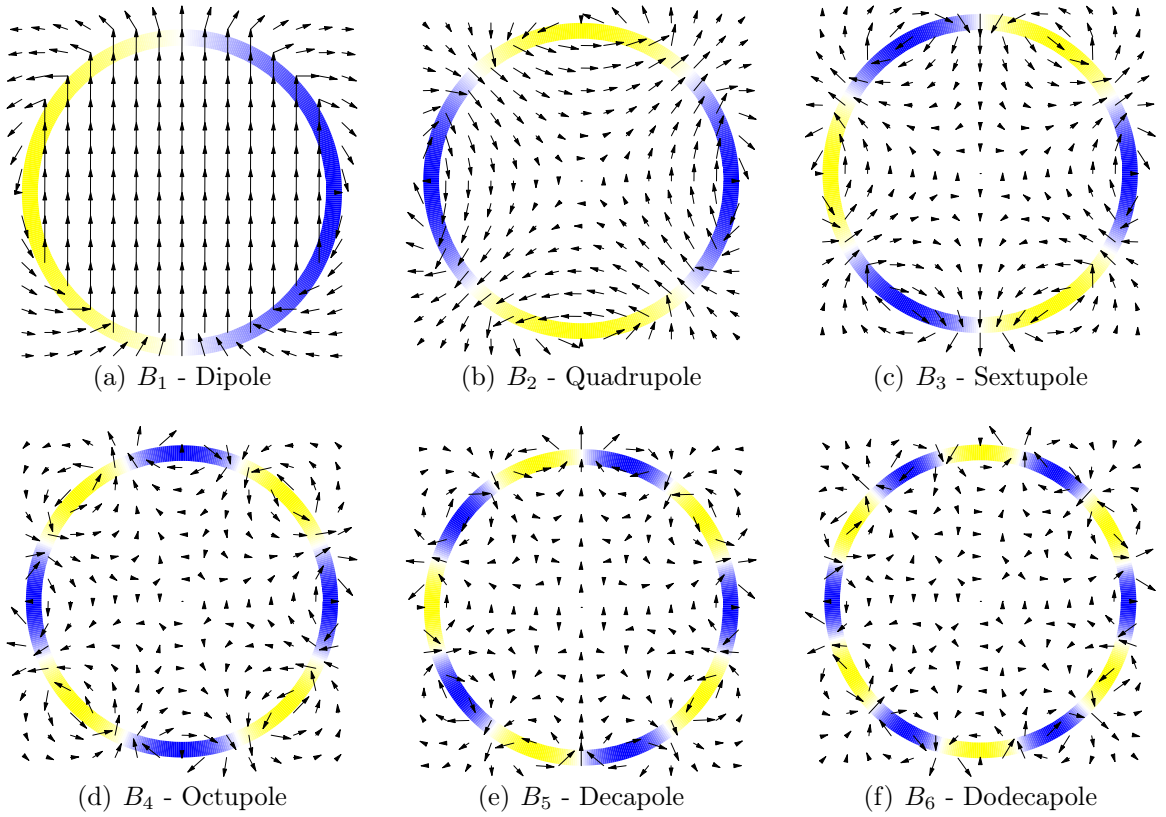


Figure 2.10: Multipoles and corresponding current distribution of the B_i ($i = 1, 2, \dots, 6$).

For control limits on the main field the so-called normalized transfer function TF_{norm} is used instead of b_1 which equals 10000 according to the definition above. The normalized transfer function [2] is given by

$$TF_{norm} = \frac{TF - TF_{nom}}{TF_{nom}} \cdot 10^4,$$

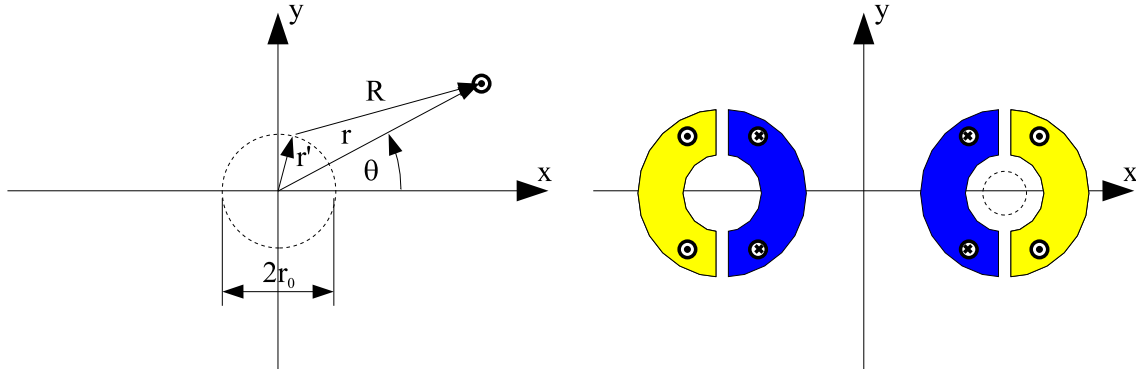
where TF is the transfer function given by $TF = B_N/I_{exc}$ and I_{exc} denotes the excitation current. TF_{nom} is a reference value given at injection current level ($TF_{nom} = 0.707 \text{ T/kA}$).

Also used is the so-called integrated transfer function TF_{int} which is given by the multiplication of the transfer function TF with the magnetic length l of the magnet ($l = 14.312 \text{ m}$ for LHC main dipole magnets [5]):

$$TF_{int} = TF \cdot l.$$

2.3.2 Geometric Field Error

For the analysis of the field quality of magnets the knowledge of the origin of certain multipole errors are inevitable. In a first assumption a magnet can be described by the sum of its conductors and therefore the created multipole errors can be derived from the multipole errors of one single filament. In fig. 2.11 a) the geometry of one arbitrary filament with respect to the reference circle is shown. The two integrals (2.6) and (2.7) can be solved for an reference radius r_0 ($r' = r_0$, $r \neq r'$) by means of a taylor series [15] but only some qualitative thoughts shall be shown here.



(a) Sketch for the calculation of geometric field error. (b) Sketch of a double aperture magnet without iron yoke in order to basically explain symmetry effects on the multipoles.

Figure 2.11: Geometric field error - analytic approach.

One single filament will excite almost all multipoles with decreasing strength for increasing distance. The angular distribution is only depending on the angle of the filament's position θ and the distance from the evaluation circle. Due to the circular nature of the field lines of a filament the normal magnetic induction $B_r(r_0, \phi)$ has one zero crossing for $\phi = \theta$ and $\phi = -\theta$. For instance for the case where the angle $\theta = 0$ then all A_n are zero as well.

Two filaments of same current with an up-down symmetry create a field of magnetic induction perpendicular to their mid-plane and with a zero normal field at $\phi = 0$ and $\phi = \pi$. As mentioned above then all skew multipoles are zero since the zero crossing can

not be described by the cosine terms. Thus an up-down symmetric geometry does not create skew multipoles.

Two filaments of opposite currents at a left-right symmetric position cause a left-right symmetric field and therefore all skew multipoles are possible outside their connection plane but only the odd normal multipoles can be produced.

Combining the last two geometries gives a geometry with no skew and only odd normal multipoles. For all geometries with these symmetries only these multipoles are to be expected.

In fig. 2.11 b) the very basic design of a double aperture magnet is shown. As can be seen the geometry is following an up-down symmetry. In reference to the dashed circle the structure has no left-right symmetry, but the even multipoles are small since they are only created by cross-talk of the coil on the left side and therefore the distance to the reference circle is bigger.

The coil is situated in an iron yoke which can be assumed in a rough estimate of circular shape and high permeability. Using the so-called imaging method the iron yoke can be expressed by the image currents of all filaments and all symmetries are conserved. With increasing excitation current the currents and image currents of all filaments increase evenly and the field error stays constant. However, the iron yoke used in the LHC main bending magnets can not be described by the imaging method. Its contribution to the magnetic field changes the overall field distribution but conserves the up-down symmetry. For this reason the normal multipoles with and without iron yoke differ but the skew multipole still do not exist.

For low local field the iron yoke can be assumed as of linear and high permeability and so the field error does not change with changing excitation current. For high values of magnetic induction the magnetization of the iron saturates. Because of the asymmetry of the iron yoke with respect to the evaluation circle within one aperture and the locally different field distribution, the left-right asymmetry is influenced and the normal multipoles are changed. The skew multipoles stay zero.

As shown in [15] the multipole errors decrease in general by the order $\propto 1/r^n$ where r denotes the distance between the filament and the center of the reference circle and n denotes the number of the multipole. The influence of the lower order multipoles is more pronounced.

Figure 2.12 shows the field error b_3 plotted versus the excitation current for all three coil cross sections. It can be seen that the value differs significantly for cross section 1 and 2 and that for high currents (above 4000 A) the iron saturation influences the shape.

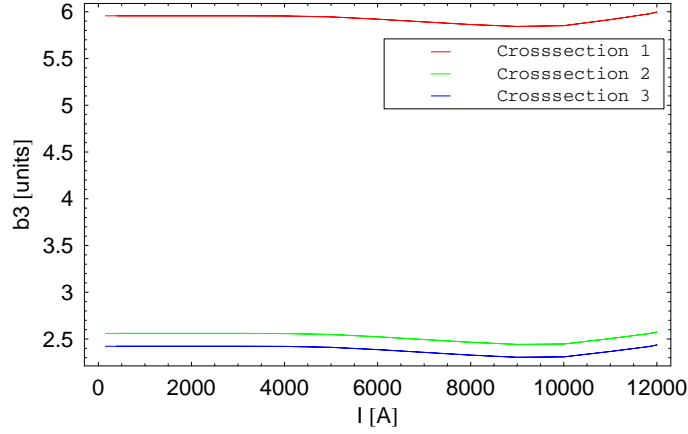


Figure 2.12: Multipole b_3 simulated without persistent currents. The shape is only influenced by the coil cross section layout and the saturation of the iron yoke.

2.3.3 Persistent Current Field Errors

Without persistent currents the field error would only change with the excitation current due to the saturation of the iron. In fig 2.13 the field error b_3 is shown as calculated with and without persistent currents. It can be seen that the hysteresis is only caused by the superconductor magnetization currents and the field error is for low excitation one order of magnitude bigger than for nominal current.

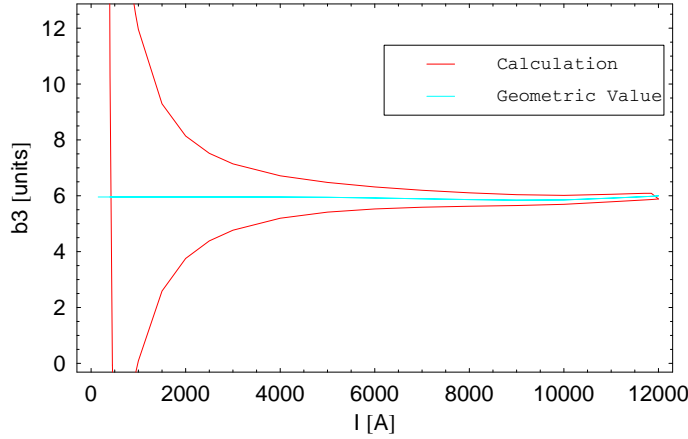


Figure 2.13: Simulation of the multipole b_3 for a magnet of coil cross section 2 with and without persistent current contribution. The calculation without persistent current contribution is denoted as the *geometric value*.

For the calculation of the expected persistent current effects on the multipoles the bipolar current layers of the filaments are replaced by ideal magnetic line dipoles of equivalent magnetic momentum. As explained in section 2.2.3 every change of the magnetic induction

is modeled by new a current layer corresponding to the field difference. The magnetic momentum of each dipole is orientated anti-parallel to this local difference of magnetic induction. In this way all symmetries are conserved when the bipolar persistent currents are added.

As shown in [19, p. 126ff] the influence of the persistent currents decreases with the order $\propto 1/r^{n+1}$ where r denotes again the distance of the filament to the center of the evaluation circle. Therefore the lower order multipoles are of higher priority. As already mentioned, the even multipoles are much smaller than the odd multipoles since they are created by cross talking between the two apertures.

Taking into account that the critical current density decreases with increasing field, the screening effect also decreases and the overall current density in each filament decreases as well. It should be noted that even for nominal current a certain number of strands stay in a low field region and therefore keep some visible superconductor magnetization. Since the multipoles are normalized by the main field, which increases in a first approximation linearly with the transport current, the persistent current multipoles also decrease with increasing field and transport current, respectively.

For this thesis the influence of the persistent currents is investigated on the multipole b_3 and later also on the higher b_5 and b_7 . The skew multipoles are never considered since the ideal magnet as assumed in the simulated geometry is perfectly up-down symmetric.

2.4 The Simulation Program ROXIE

For the simulation of the LHC magnets the field calculation program ROXIE⁵ was developed at CERN. Based on the geometry data of the cable, coil cross section and iron yoke the magnetic field produced by the superconducting coil can be calculated either in 2D or in 3D.

For the basic calculation of the coil field without persistent currents the strands are replaced by line currents and the magnetic induction is calculated by means of Biot-Savart's law.

For the calculation of the magnetic material the so-called BEM⁶-FEM⁷-coupling method is used which allows a considerable reduction of the number of finite elements compared to standard FEM-codes. According to this method wide air areas at the coil ends and more relevant the coils are not modeled in finite elements but considered by expressing the magnetic field on the boundary. This reduces the number of elements needed and for the coil it especially increases the precision of the field since the conductors can be described more precisely. The field created by the iron material is superimposed to the field of the superconducting coil.

As shown in section 2.2.3 the persistent currents depend on the local magnetic field. In the area of the conductors the field representing the repercussion of the iron material is superimposed to the field of the filaments by means of the BEM and therefore can be expressed for any position within the coil.

Due to the huge number of filaments the model of Völlinger is applied on strand level only. It is assumed that the local magnetic induction does not vary strongly over one strand's cross section and so the effect of the filaments can be taken into account by calculating one center filament and weighting the result with the area of the strand cross section. The field produced by the persistent currents is iterated until the induced current density of the first layer matches the resulting external field.

The three calculation steps, magnetic field produced by the coil, magnetic field produced by the magnetization of the iron yoke and magnetic field produced by the persistent currents, are repeated for each excitation current.

In order to obtain conditions similar to the operating conditions of the LHC magnets, a precycle of the current ramping has to be performed. During the first up-ramp of the transport current the strands transit from the state without any persistent currents to a fully penetrated state. Since the local field varies very much across the magnet cross section the current should be ramped up to nominal current in order to fully penetrate the maximum number of strands positioned in the low field areas as well.

According to the model of superconductors the total available current density is limited by the maximum critical current density. This has to be shared by the transport or exciting currents and the induced persistent currents. For a given transport current the persistent currents are limited and so the screening decreases with increasing transport current. So the

⁵**R**outine for the **O**ptimization of magnet **X**-sections, **I**nverse field calculation and coil **E**nd design

⁶**B**oundary **E**lements **M**ethod

⁷**F**inite **E**lements **M**ethod

field errors are reduced again with increasing transport current. Because of the reduction of screening for high currents additional quenches can be produced for high field strands.

ROXIE superimposes the effects of transport currents and persistent currents assuming the critical current density to be much bigger than the transport current density.

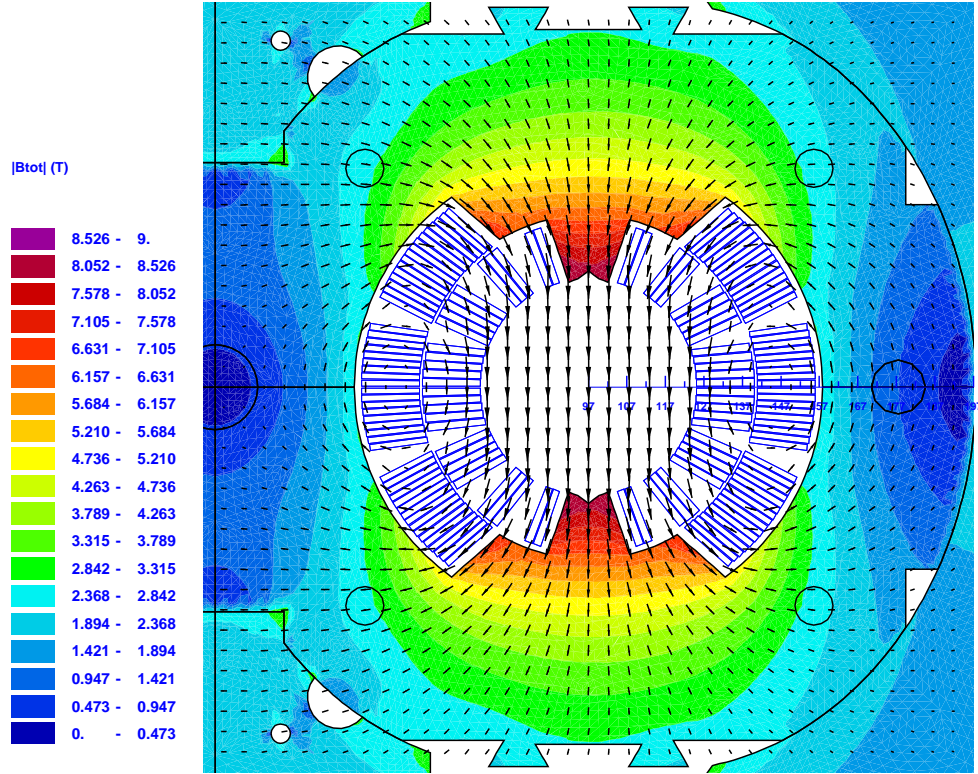


Figure 2.14: Simulation results of a LHC main bending magnet with coil cross section 1 at nominal field level. The colors indicate the modulus of the magnetic induction in the iron parts like the collar made of stainless steel and the iron yoke. The arrows represent the magnetic induction. The coil is only represented by the blue outlined white areas. The aperture shows the wanted dipole field. Considering the boundaries of the different colors one can see the slight left-right asymmetry.

2.5 Superconductor Magnetization

The model presented in section 2.2.3 depends on a function for the critical current density for each modeled type of filament. According to the critical state model, shown in section 2.2.1, each filament carries always the maximum possible current density matching the applied local magnetic field and temperature. This way, values for the critical current density can be indirectly experimentally determined. The induced current is in general not directly accessible and can only be measured indirectly by its magnetic effect on a pick-up-coil. Performing a measurement with an applied changing magnetic field, the field of the persistent currents can be measured versus the magnetic flux. Because the persistent currents do not decay with time no currents are induced if a static field is applied. After cancelling the excitation from Eq. (2.8) the magnetization of the specimen can be obtained.

$$\vec{H} = \frac{1}{\mu_0} \vec{B} - \vec{M}. \quad (2.8)$$

Magnetization and current density in general are related by Eq. (2.9) and so the superconductor magnetization \vec{M} is given by the local change of the current density \vec{J} . Further the local distribution of \vec{J} within a filaments cross section is given by the used model and so the function of critical current density of local magnetic flux density can be calculated as shown in [19, p. 60f].

$$\vec{M} = \vec{\nabla} \times \vec{J}. \quad (2.9)$$

2.5.1 Measurement of Superconductor Strand Magnetization

The measurement of magnetization can not be performed on a single filament since the material is far too brittle to be handled mechanically and would break. For this reason only strands are measured for all cables. This modus operandi comes along with some averaging effects especially for high magnetic field because of the big number of filaments and a locally varying magnetic field across the strand cross section.

Following [10] and [11], the basic principle of the integrating coil magnetometer magnetization measurement will be explained.

In the area of homogeneous field of a big excitation coil two pick-up-coils are put symmetrically with respect to the mid plane. In one of them the superconducting sample is put perpendicularly to the field (see fig. 2.16).

If, for example, the current in the excitation coil is ramped up, the flux in the two pick-up coils rises and induces a voltage drop across their leads. In order to expel the applied magnetic field, persistent magnetization currents are induced in the sample and cause a change of the magnetic field in the surrounding pick-up-coil. Since the external magnetic field varies with time the persistent currents are also following the varying magnetic field and so their influence can be seen on the induced voltage drop across the pick-up-coil.

The voltage drop induced by the excitation field can be cancelled out by subtracting the two pick-up-coil voltages since one of them only sees the external field. Integrating the so obtained voltage over time gives the magnetic flux as function of time and so for



(a) Test station with down cryostat and probe holder. The magnet is below the platform.



(b) The long metal shaft contains the strands to be measured. The big tank is filled with super fluid helium in order to provide the measurement temperature of 1.9 K for suitable time span.

Figure 2.15: Test station for superconductor magnetization (Pictures with the courtesy of S. Le Naour).

a known coil geometry the magnetic flux density can be derived. Combining this result with the used excitation function and the permeability of the surrounding linear medium (vacuum, air or liquid helium) gives the magnetic field as function of the applied magnetic flux density.

$$\begin{aligned}
 \frac{d\Psi}{dt} &= - \oint \vec{E} d\vec{s} = U_i \\
 \Leftrightarrow \Psi &= \int U_i dt + C = f(t) + C \\
 \Leftrightarrow B &= \frac{f(t = B \cdot t_0 / B_e)}{A_{pickup}} + C^* \\
 \Leftrightarrow H &= \frac{f(B)}{\mu_0 A_{pickup}} + B_0.
 \end{aligned}$$

Here Ψ denotes the magnetic flux through one pick-up coil with area A_{pickup} and U_i the induced voltage at its leads. The function $f(t)$ or $f(B)$ is the function in which one is

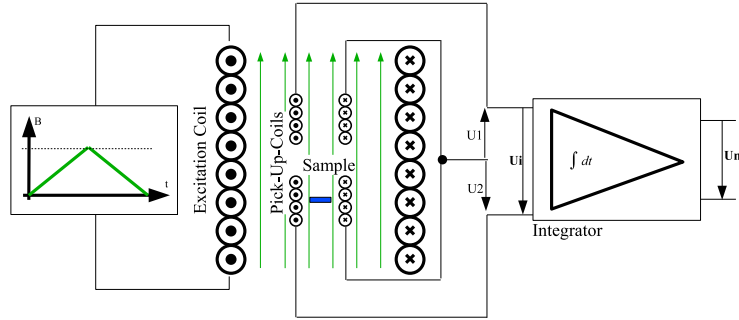


Figure 2.16: Principle of magnetization measurement.

interested. The ramp rate of the exciting field is given by $B(t) = B_e/t_0 \cdot t$ which can easily be inverted.

All measurements start with the so-called virgin curve where the superconducting sample is exposed to a magnetic field for the first time since cooling down. Since for zero field at working temperature (e.g. 1.9 K) no magnetization current is induced in the sample, i.e., the virgin curve determines also the offset or integration constant B_0 to zero.

After a precycle all filaments are in a defined state and then the magnetization is measured for different loops of field strength. Exemplary results of magnetization measurement for different field loops are shown in fig. 2.17. The sharp edges for minimum and maximum field of one loop are caused by the sudden change from fully penetrated into low penetrated state. The characteristic form of the curve is caused by smoothening effects among all filaments seeing different magnetic flux densities and screening each other. This feature is included in the used magnetization model and has not to be considered during the further work. For one single filament the transition from the rising branch to the falling branch would be much more rapid and thus causing an even sharper edge.

2.5.2 Superconductor Magnetization for Different Manufacturers

Before a cable is produced a unit sample of strand production is tested at CERN. According to the measured superconductor magnetization curve the strands for the cables are combined in order to meet the needs of cable magnetization for the LHC. Since one cable consists of 28 or 36 strands the differences in magnetization of one manufacturer can be diminished by combination and so the strands with a problematic magnetization profile can be averaged out. For this reason for each company only the average magnetization curve of all up to now measured strands is stored.

Although a slight difference in the rising and falling branch of the magnetization loop can be seen in fig. 2.17, only the falling branch is taken into account for the following studies. In a further examination reasons for the differences in up and down ramp, like e.g. a small Meissner-phase or slight diamagnetic influence of the copper parts on the overall observed magnetization could be discussed.

As mentioned in section 2.5.1 close to the turning point of the exciting magnetic field

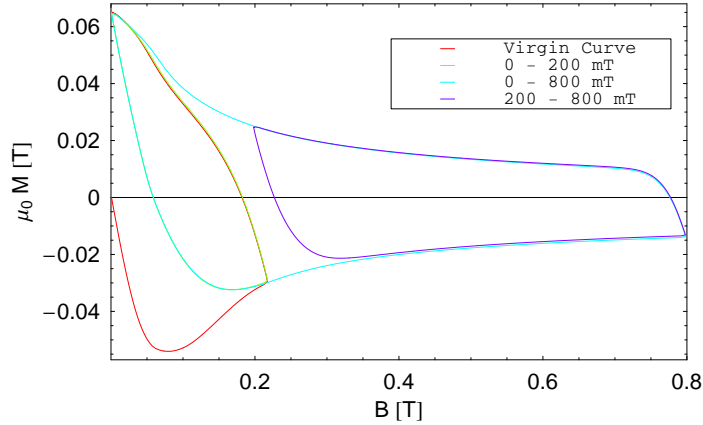


Figure 2.17: Results of magnetization measurement for strands for the inner cable 01E. The measurement starts with the virgin curve in the origin (red) and continues in counter clock wise loops. For the following the upper branch of the loop covering the region from 0 to 800 mT is used. All data is given by S. Le Naour

the superconductor magnetization is influenced by the grade of penetration amongst the filaments and is therefore not representative for the overall critical current density. The effect causing the limited peak for a field close to zero is not yet understood and therefore the program does not use the magnetization/critical current function for extremely low field values around zero. For the fit of the critical current density the values close to both ends of the curve are omitted.

In fig. 2.18 the remaining branch of the magnetization versus the applied magnetic flux density for all used cables is shown and rather big differences can be noticed easily.

2.5.3 Conversion of Superconductor Magnetization into Critical Current Density

According to the critical state model a superconductor carries always the maximum current density matching its temperature and surrounding magnetic field. For relatively small values of magnetic field a single filament is already fully penetrated and the local distribution of magnetization current density stays constant and varies only in its absolute value with the change of flux density for the rest of the loop's branch. The relation between magnetization and critical current density is derived in [19, p. 60f] and can be expressed for a fully penetrated filament by Eq.(2.10). The negative sign denotes the opposing behavior of the induced current compared to normal conducting magnetic materials.

$$M_f = -\frac{4}{3\pi} r_f J_c. \quad (2.10)$$

The measured magnetization for a strand has to be scaled down to one filament of the model. Assuming the strand behaving like one thick filament of low density the magneti-

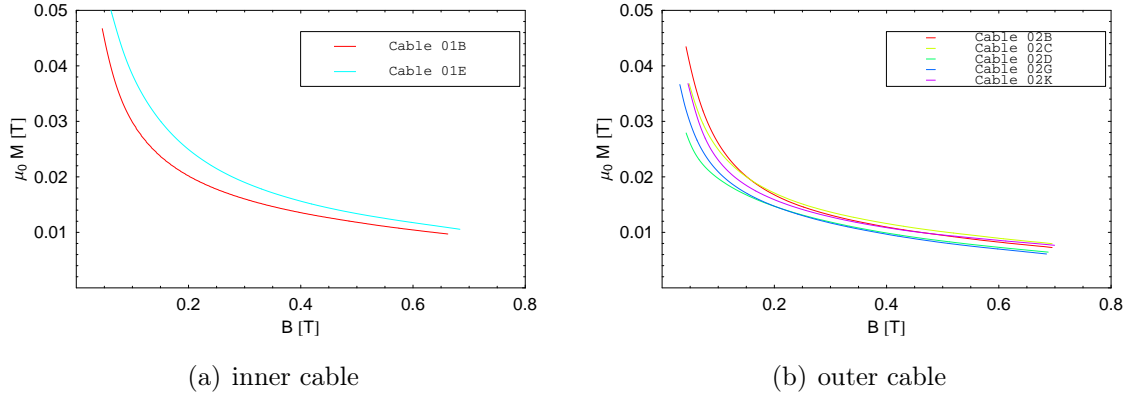


Figure 2.18: Superconductor magnetization of the upper (falling) branch for all manufacturers. All data given by S. Le Naour.

ization for a strand can be easily converted into magnetization of a filament by comparing the densities. The conversion factor is given by the ratio of superconducting area $N_f A_f$ over total area of a strand A_s where N_f denotes the number of filaments.

$$M_s = M_f \frac{N_f A_f}{A_s}.$$

With Cu/Sc the copper to superconductor ratio this yields

$$\frac{N_f A_f}{A_s} = \frac{1}{1 + \frac{Cu}{Sc}} = \lambda.$$

Where λ denotes the filling factor, Eq. (2.10) can be written for strands as:

$$M_s = -\frac{4}{3\pi} r_f \lambda J_c. \quad (2.11)$$

Since the measurement data is given in Tesla, Eq. (2.11) has to be multiplied by the permeability of empty space μ_0 to convert magnetization data into critical current density. With the values given in tab. 1.2 for inner and outer layer, the measurement can be converted.

2.6 Cold Measurement of Magnets

As mentioned above the field quality of the dipole magnets has to fulfill very high requirements and so every magnet has to pass certain tests in order to be accepted at CERN for the LHC.

During the production process the magnet is measured twice at warm conditions (room temperature) at the producing companies once after collaring and once after welding into the cold mass. The measurement data can be extrapolated to cold conditions (at 1.9 K) by CERN and so production errors can be found in an early state. Since the warm measurement is performed with a low current of approximately 10 A and all superconducting cables are in non superconducting state the measurement is limited to the field errors produced by the coil geometry. Persistent current and iron saturation effects can not be measured at this point, but e.g. misalignments of conductor blocks can be seen and the problem can be inversely calculated from the measurement data.



Figure 2.19: Test stand for cold measurement with two dipole magnets (blue).

The equipment for cold measurements at 1.9 K is very expensive and only in use at CERN. According to the acceptance policy approximately up to one third of the cryo-dipoles is measured magnetically at cold conditions. 100% of the magnets are tested for quench behavior. The aim of these tests is to guarantee [16] that the cryo-magnets meet the specifications related to the cryogenic, vacuum and electrical integrity, to the capacity to reach nominal (8.33 T) and ultimate field (9 T) levels after a maximum specified number of quenches, to the efficiency of the magnet protection and to the quality of the field. In the same way information for the installation and positioning of the cryo-magnet in the ring and for the operation of the machine are obtained e.g. the magnets are arranged in the ring such that the integrated field error of the machine is sufficiently small.

2.6.1 The Field Quality Measurement

During the cold test [3] the beam pipe is equipped with an anticryostat where two 16 m long shafts are introduced. These shafts consist of 13 ceramic sections representing one measurement range and each containing two tangential coils and one dipole compensation coil. In this way the field quality can be measured at 13 averaged positions along the magnet at the same time.

Figure 2.20 shows the cross section of a shaft. For the measurement only one tangential coil is needed. The second is used for checking the measurement, spare and rotational symmetry. With the centered compensation coil the dipole field can be subtracted from the tangential measurement in order to increase the sensitivity for the higher multipoles.

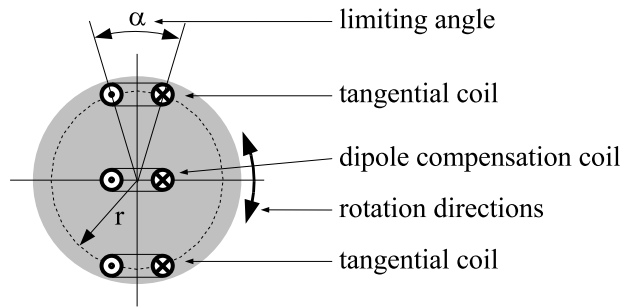


Figure 2.20: Principle of cold measurement shafts.

According to the theory of multipole expansion of an arbitrary magnetic field, the field along the measurement circumference can be expressed by its multipole coefficients producing a periodic field along the measurement circle. The tangential coil can not resolve multipoles with a periodic length smaller than the coil width. The maximum resolvable multipole is thus given by $n_{max} = 2\pi/\alpha$. For the used coil the maximum resolution for multipoles n_{max} is 12.5.

For the measurement for each set current the two shafts perform one revolution in each direction and average the measured value for each position.

2.6.2 Current Ramp Cycle

Directly after the cool down the filaments are not magnetized under field and current free conditions. Increasing the current produces a filament magnetization which results in field errors that follow the so-called virgin curve. For the operation of the machine these errors are of no importance, however, the filaments have to be in a pre-defined state with respect to their hysteresis and therefore a so-called precycle is performed before each measurement. After the precycle which is basically a fast up and down ramp all filaments are in a defined state.

For the measurement [17] the current is ramped up from 400 A to nominal current (11850 A) and down again in 35 steps. Each step builds a plateau of 140 s. In fig. 2.21 the ramp cycle including the precycle is shown (injection current is 760 A).

In order to match with the measurements the same current ramp cycle is used for the simulation. Small deviations in the current settings during the measurement compared to the simulation are then linearly interpolated.

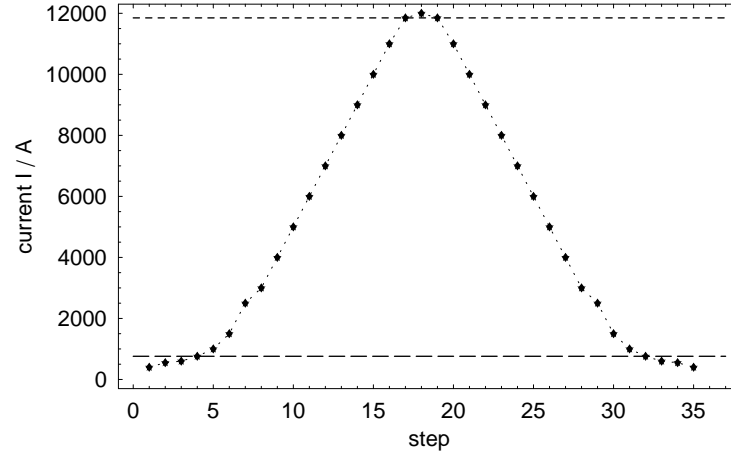


Figure 2.21: Current ramp cycle taken from cold magnet measurement. The lower dashed line indicates the current for injection and the upper dashed line indicates the current for nominal field. In addition to the specified values the current is ramped up to 12000 A. The same ramp cycle is used for the simulations.

3 Fit Function for the Critical Current Density

In general the critical current density of superconducting strands is expected to be dependent on the locally applied magnetic flux density, operating temperature, the applied strain and radiation exposure. For all these different quantities functions, which describe these influences and which are probably nested, have to be found in order to calculate the critical current density.

For this thesis only the field dependence of the critical current density is investigated. The dependence on radiation exposure is totally neglected. The influence of strain is set to be constant, although it is known that it should be differentiated between strain applied during the drawing process of the strand, strain applied while bending the turns of the magnet and strain applied by the Lorentz forces during operation of the magnet. The leading two cannot be seen in magnetization data of strands apart from a constant but are expected to influence the magnet behavior.

The superconducting state is limited by temperature and magnetic flux density values given by

$$B_{c2(T)} = B_{c20} \left(1 - \left(\frac{T}{T_{c0}} \right)^n \right) \quad (3.1)$$

where B_{c20} denotes the upper critical field for zero temperature, T_{c0} denotes the upper critical temperature for zero field and the exponent n is a fit parameter. This function was originally published by Lubell [13] where he sets the fit parameter to $n = 1.7$ for best results although - quoting the author - the theoretical value would be 2. The boundary of the superconducting state is given by Eq. (3.1) and can be seen in fig. 3.1.

For the direct influence of the temperature on the critical current density a linear function was given by Lubell for high fields [13], a bell-shaped squarish function $(1 - (T/T_{c0})^2)^2$ was given by Summers [18] and both approaches were finally adapted by Bottura to

$$J_c \propto (1 - (T/T_{c0})^n)^\gamma \quad (3.2)$$

with $n = 1.7$ like in [13] and γ being a fit parameter. For this thesis the function given by Eq. (3.2) is used together with a constant fit parameter γ .

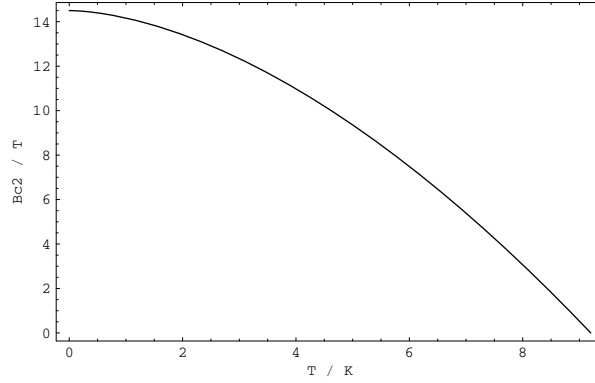


Figure 3.1: Dependency of the upper critical flux density B_{c2} on temperature. The function gives the boundary of the superconducting state.

3.1 Scaling Power Law

In [4] L. Bottura published a power law fit function which gives the critical surface for NbTi superconductors as function of applied magnetic flux density and temperature.

$$J_c(B, T) = J_{ref} \frac{C0}{B} \left(\frac{B}{B_{c2}(T)} \right)^\alpha \left(1 - \frac{B}{B_{c2}(T)} \right)^\beta \left(1 - \left(\frac{T}{T_{c0}} \right)^n \right)^\gamma. \quad (3.3)$$

J_{ref} denotes a reference critical current density in order to take the unit of measurement and to reduce the magnitude of $C0$. It is given by the measured critical current density at 4.2 K and 5 T [9]. $B_{c2}(T)$ gives the upper critical magnetic flux density as shown in Eq. (3.1) and therefore it defines the location of the zero crossing.

With the parameters α , β and $C0$ the function can be adapted to measurements versus magnetic induction for fixed temperature and with γ and again $C0$ to measurements versus temperature for fixed field. The values for the fit parameters and the assumed range given in [4] are shown in tab. 3.1.

Table 3.1: Parameter range and calculated values for the scaling power law by L. Bottura.

Parameter	Given Range	Shown Values
$C0$	–	(21.7 to 37.7)
α	0.5 to 0.8	(0.57 to 0.89)
β	close to 1	(0.64 to 1.1)
γ	close to 2	(1.73 to 2.3)

It should be mentioned that a function similar to Eq. (3.3) with fixed exponents was published by Summers in [18]. In tab. 3.2, the parameters used by Summers in terms of Bottura's function are shown.

Table 3.2: Parameters of Summers' approach in terms of the scaling power law.

Parameter	Value
$C0$	$C\sqrt{B_{c2}(T)}$
α	0
β	2
γ	2
n	2

3.1.1 State of the Art

Up to now the scaling power law was used for all simulations with one set of parameters for both inner and outer cable of all manufacturers. The parameters (shown in tab. 3.3) were determined by Völlinger in [19] and not further investigated. This will be denoted as the unspecific fit in the following.

Table 3.3: Parameters for the unspecific fit by Völlinger.

Parameter	Value
$C0$	27.04 T
α	0.57
β	0.9
γ	2.32
n	1.7

The wide variance of the measured magnetization as shown in fig. 2.18 is not represented and the deviation between measured data and the unspecific fit should be shown explicitly in fig. 3.2 for an used combination of inner and outer cable like 01B 02K. Converting the critical current density J_c into magnetization by means of Eq. (2.11) yields two different conversion factors since inner and outer cable differ in filament diameter and filling factor.

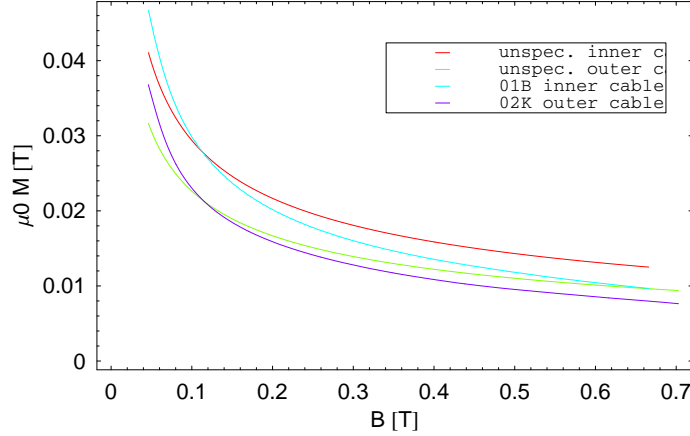
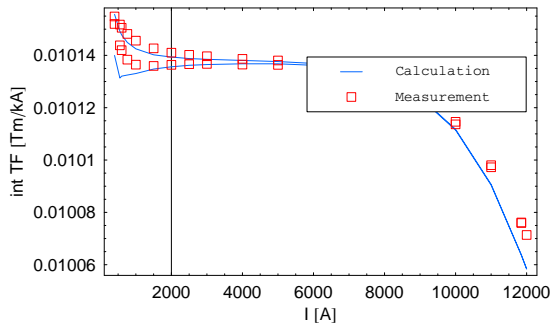


Figure 3.2: The unspecific standard critical current density (scaled as magnetization) in comparison to the measured magnetization of two cables used in combination. The measured magnetizations show big differences in curvature and slope which is not represented by the unspecific fit because it differs only by a constant factor. The magnetization measurement data is given by S. Le Naour. The fit parameters are taken from [19].

In fig. 3.3 the most important multipoles for LHC main dipole magnets are shown in case of the unspecific approach in comparison to the cold measurement results of one magnet. The matching of the even multipoles is already satisfying since they are generally more influenced by iron effects than by the critical current function. On account of this the even multipoles are not further investigated for the critical current fit. The results for the odd multipoles show a rather big deviation and the calculated hysteresis width varies a lot.



(a) integrated Transfer Function.

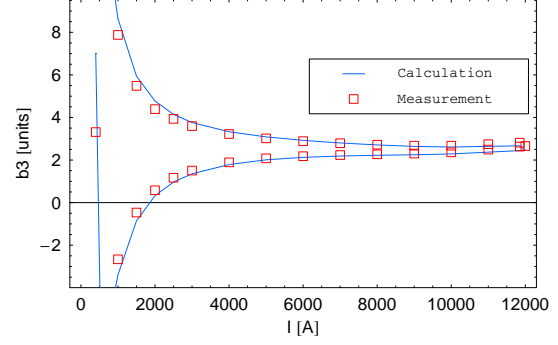
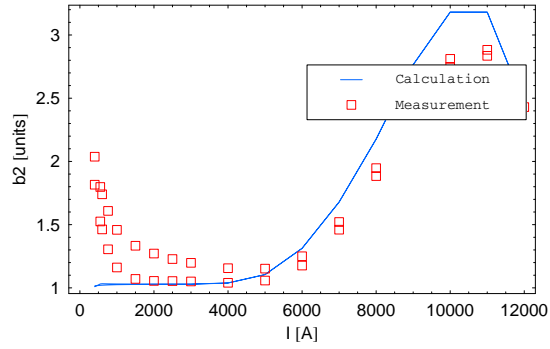
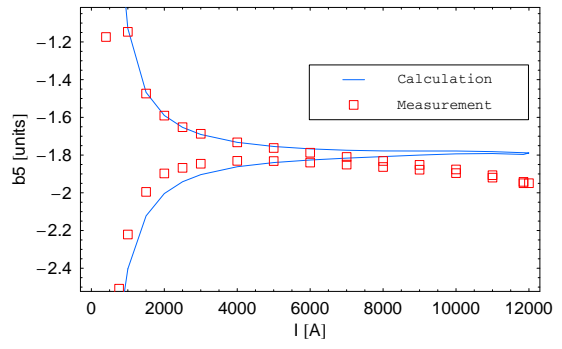
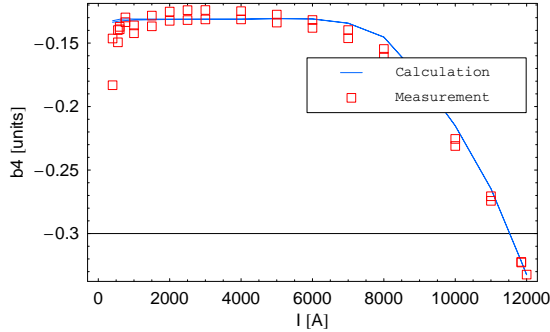
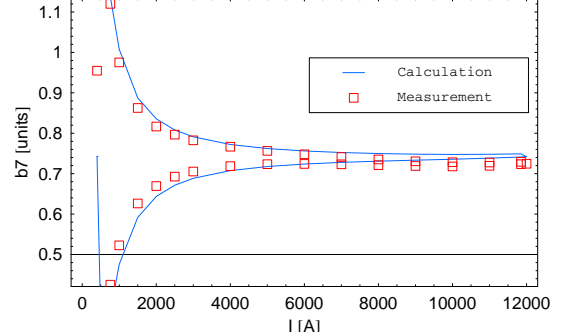
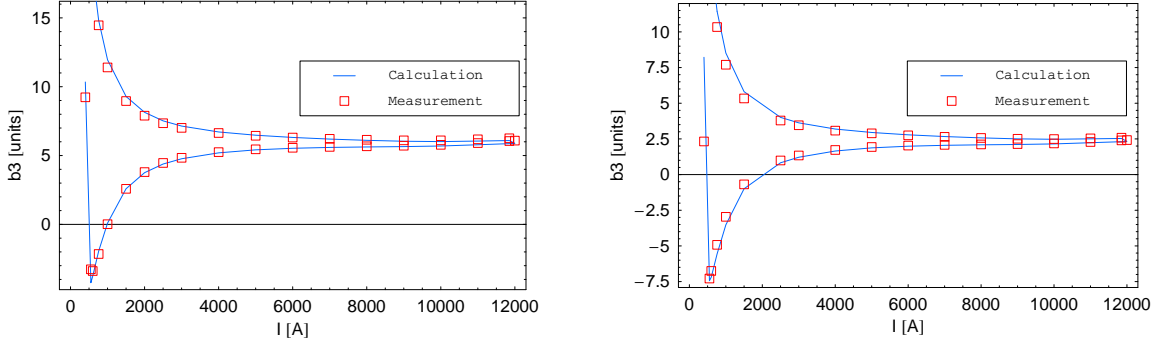
(b) Normal multipole b_3 .(c) Normal multipole b_2 .(d) Normal multipole b_5 .(e) Normal multipole b_4 .(f) Normal multipole b_7 .

Figure 3.3: Simulation results for the lower order multipoles resulting from the approach with the unspecific fit function and the parameters from [19] in comparison to the cold magnetic measurements of magnet number 3043 equipped with coil cross section 2 and cable combination 01B 02K. Measurement data given by S. Sanfillippo.

In fig. 3.4, the b_3 of two magnets with different coil cross sections and cable combinations are shown in order to demonstrate the need of an individual adaptation of the fit function for all cables. Comparing all three plots for b_3 shows the different grade of matching and such demonstrates the differences between the used cables.



(a) Magnet number 2009 with coil cross section 1 and cable combination 01B 02C.

(b) Magnet number 3090 with coil cross section 3 and cable combination 01B 02G.

Figure 3.4: Simulation results for normal multipole b_3 of the approach with the unspecific fit function and parameters from [19] in comparison to the cold magnetic measurements given by S. Sanfillippo.

3.1.2 Analysis of Sensitivity

Before adapting the parameters to the given data sets a first analysis of parameter sensitivity will be done in order to obtain a theoretical background of the specific influence of each parameter. Moreover a deeper understanding of the general influence of the critical current density on the field errors can be achieved.

The function (3.3) can be adapted to the measurement values by means of five different parameters. Keeping the temperature constant the number of fit parameters reduces to three: $C0$, α and β . The exponents γ and n can be kept constant at the values given in tab. 3.3.

Starting with the unspecific fit parameters from section 3.1.1 each parameter is varied on a suitable range and the critical current density function is plotted. Furthermore the field errors of a magnet using the same fit for inner and outer layer are computed and shown for the multipole b_3 which is the most sensitive.

As can be seen in fig. 3.5 a) the parameter α influences the critical current density mainly in the region of low field. With decreasing α the current density rises more strongly. The simulation results show the same behavior. With decreasing α the hysteresis width increases. The effect is mainly visible for low excitation currents.

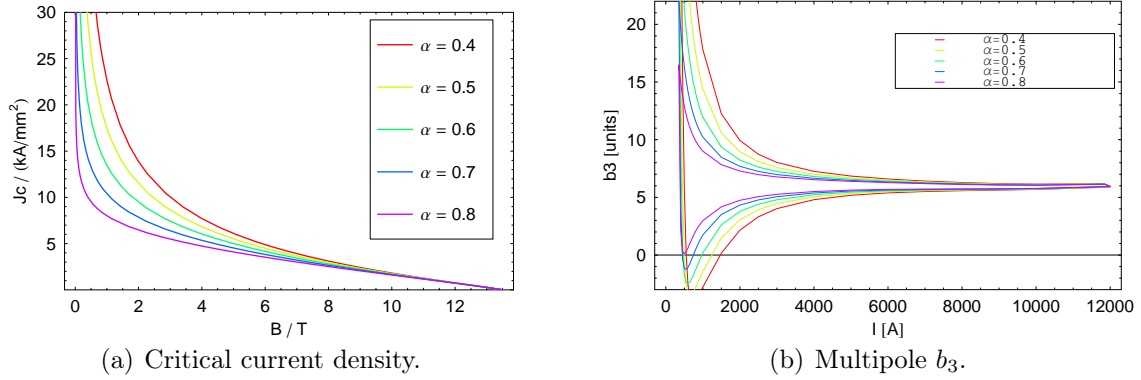
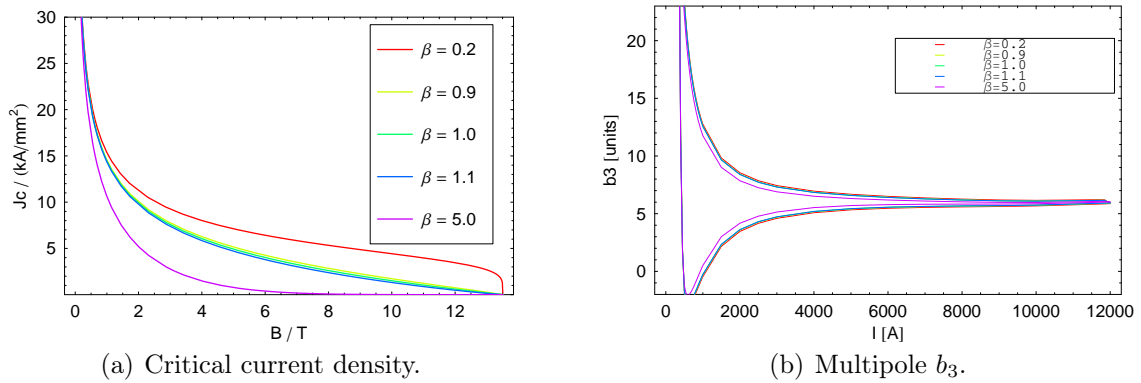
Figure 3.5: Influence of fit parameter α on the scaling power law.

Figure 3.6 shows the influence of β . Here with decreasing parameter value β the critical current density increases for high field. This effect is not very pronounced for values of β close to 1 but for much higher or smaller values it is significant. For the simulation results the multipole is in general very little influenced by β and only the two extreme values are distinguishable. For very high β the multipole is reduced up to very low currents. The hysteresis width at injection current is not significantly influenced for all values of β .

Figure 3.6: Influence of fit parameter β on the scaling power law.

In fig. 3.7 the influence of the linear constant C_0 is shown. For the critical current density an increase of the values of C_0 causes an increase of the function over the whole range. This can be noticed in the simulation results, too. In a first approximation doubling the value of C_0 doubles the value of the b_3 multipole created by the persistent currents. The geometric value stays constant.

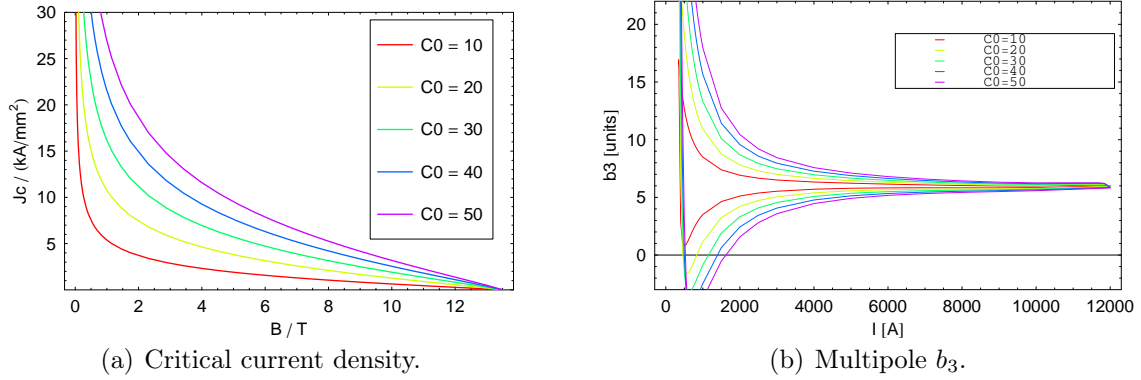


Figure 3.7: Influence of fit parameter $C0$ on the scaling power law.

Most interesting fact from this analysis is that an increase of the critical current density for high field values, as could be done by the parameter β , does not cause a significant increase of the multipole b_3 . This reinforces the assumptions from section 2.3.3.

3.1.3 Adapting Parameters to Different Cables

For the adaptation of the fit parameters to different cable measurements, the function (3.3) should be converted into magnetization data unless the available data already comes from magnetization measurements. As shown in section 2.5.3 the relation between both quantities is given by a constant factor and so the conversion can be done in both directions very easily.

Method

A practical method to find the fit parameters for a given function is to use the linear regression method shown in the appendix B.2 but in order to do so an approach with linear coefficients is needed. Since the fit function consists of three exponential terms connected by multiplication, it is not difficult to transform the approach by applying the natural logarithm in a sum of linear terms.

$$\begin{aligned}
 M(B, T) &= M_{ref} \frac{C0}{B} \left(\frac{B}{B_{c2(T)}} \right)^\alpha \left(1 - \frac{B}{B_{c2(T)}} \right)^\beta \left(1 - \left(\frac{T}{T_{c0}} \right)^n \right)^\gamma \\
 &\Downarrow \\
 \tilde{M}(B, T) &= \tilde{K} + \tilde{\alpha} \ln \left(\frac{B}{B_{c2(T)}} \right) + \tilde{\beta} \ln \left(1 - \frac{B}{B_{c2(T)}} \right).
 \end{aligned} \tag{3.4}$$

With

$$\begin{aligned}
 \tilde{K} &= \ln(M_{ref}) + \ln(C0) - \ln(B_{c2(T)}) + \ln \left(\left(1 - \left(\frac{T}{T_{c0}} \right)^n \right)^\gamma \right), \\
 \tilde{\alpha} &= \alpha - 1, \\
 \tilde{\beta} &= \beta.
 \end{aligned}$$

Doing the same to the dataset of magnetization, the constants $\tilde{\alpha}$, $\tilde{\beta}$ and \tilde{K} can be determined. From these the original constants can be obtained as:

$$\begin{aligned} C0 &= e^{\tilde{K}} \frac{B_{c2}(T)}{M_{ref} \left(1 - \left(\frac{T}{T_{c0}}\right)^n\right)^\gamma}, \\ \alpha &= \tilde{\alpha} + 1, \\ \beta &= \tilde{\beta}. \end{aligned}$$

The fit was performed and the standard deviation was minimized for the logarithmic data which does not necessarily mean that the standard deviation for the normal data is also at minimum. Performing a second linear regression with the found parameters and the fit function in order to determine an additional multiplicative constant C_{help} gives the final fit.

$$C0_{final} = C0 \cdot C_{help}.$$

The so obtained constant differs significantly from 1. The complete fit shows a pleasant matching.

Results for Magnetization

In table 3.4 the determined fit parameters and the standard deviation as an index of matching for all cables (see appendix B.1) are shown. In evidence the range of $C0$ is much bigger than given by Bottura in [4] and it can be seen that the values for β are by far not close to 1.

Table 3.4: Parameters and standard deviation for specific scaling power law.

	01B	01E	02B	02C	02D	02G	02K
α	0.455	0.412	0.408	0.500	0.690	0.586	0.462
β	2.015	3.481	2.308	3.464	11.70	9.671	1.077
$C0$	15.86	16.55	14.22	21.61	46.26	29.33	16.45
$\sigma \cdot 1000$	0.146	0.165	0.151	0.090	0.086	0.164	0.207

In fig. 3.9 the matching of the fit function with the magnetization data for three cables with very different fit parameters are shown.

In fig. 3.8 the fit for all cables is shown versus the magnetic induction up to the upper critical field $B_{c2}(1.9\text{ K})$. As discussed before in section 3.1.2 the high values for the parameter β cause low current densities for high fields of magnetic flux density. Especially for the cables 01D and 01G this will cause small hysteresis widths at nominal current level.

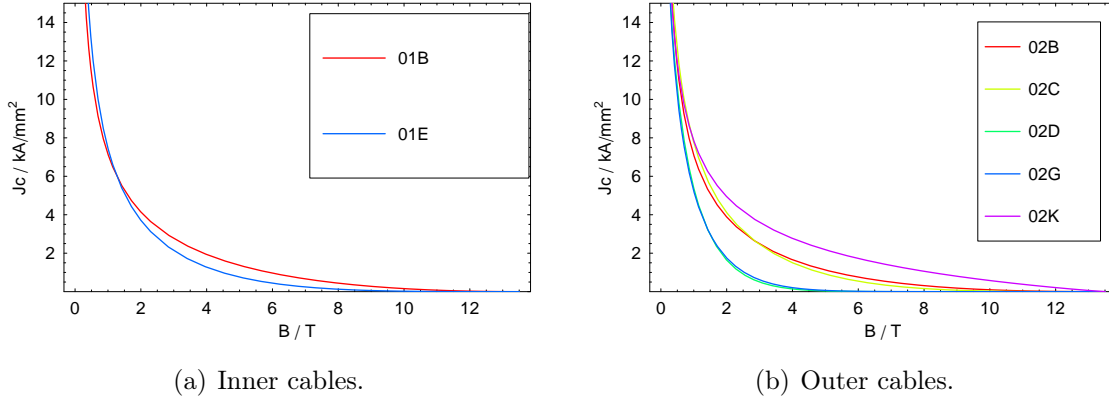


Figure 3.8: Functions of the obtained fit for inner and outer cables plotted versus magnetic induction up to the upper critical field $B_{c2}(1.9\text{ K})$. The magnetization measurement data is only available up to 0.8 T.

Results for Simulated Magnets

In figs. 3.10 a) to c) the simulation results for the multipole b_3 are shown for three different cable combinations and magnet cross sections. As expected the quality of matching with the measurement results decreases with increasing β and increasing current. Therefore it is best for the cable combination 01B 02K with $\beta \approx 1$ on the outer layer.

For excitation currents up to approximately 1500 A most strands are expected to be exposed to a magnetic induction in the range of $0 \rightarrow 1$ T. For this range the magnetization was fitted and gives best results compared to the rest of the hysteresis loop. With increasing current more and more magnetization current in more and more strands is pinched off by the high β and so the hysteresis width is reduced.

Discussion

These results give strong reasons to investigate the effects of magnetization for high field and to change the fit function in a way that yields higher current density for higher field.

Especially for β in a range of $8 \rightarrow 12$ the critical current density is for high currents of the same magnitude as the transport current density. As mentioned in 2.4 this is expected to create further perturbations.

3.1.4 Unphysical Behavior within the Given Parameter Range

As seen in the last paragraph the parameter β of the scaling power law function strongly influences the width of the hysteresis loop when it is varied over a range from 1 to 10. On strand level high values cause a bigger falling slope of the magnetization curve for low fields and so they are necessary to adapt the curvature to the data.

Investigating the behavior of the function for values close to the upper critical field shows three different types of slope depending on β .

$\beta < 1$ The part of the critical current density which depends on β is a root like function and so it has a vertical slope when the upper critical magnetic flux density B_{c2} is reached.

$\beta = 1$ The term with zero crossing at the upper critical field B_{c2} reduces to a straight line. The slope is influenced by all fit parameters.

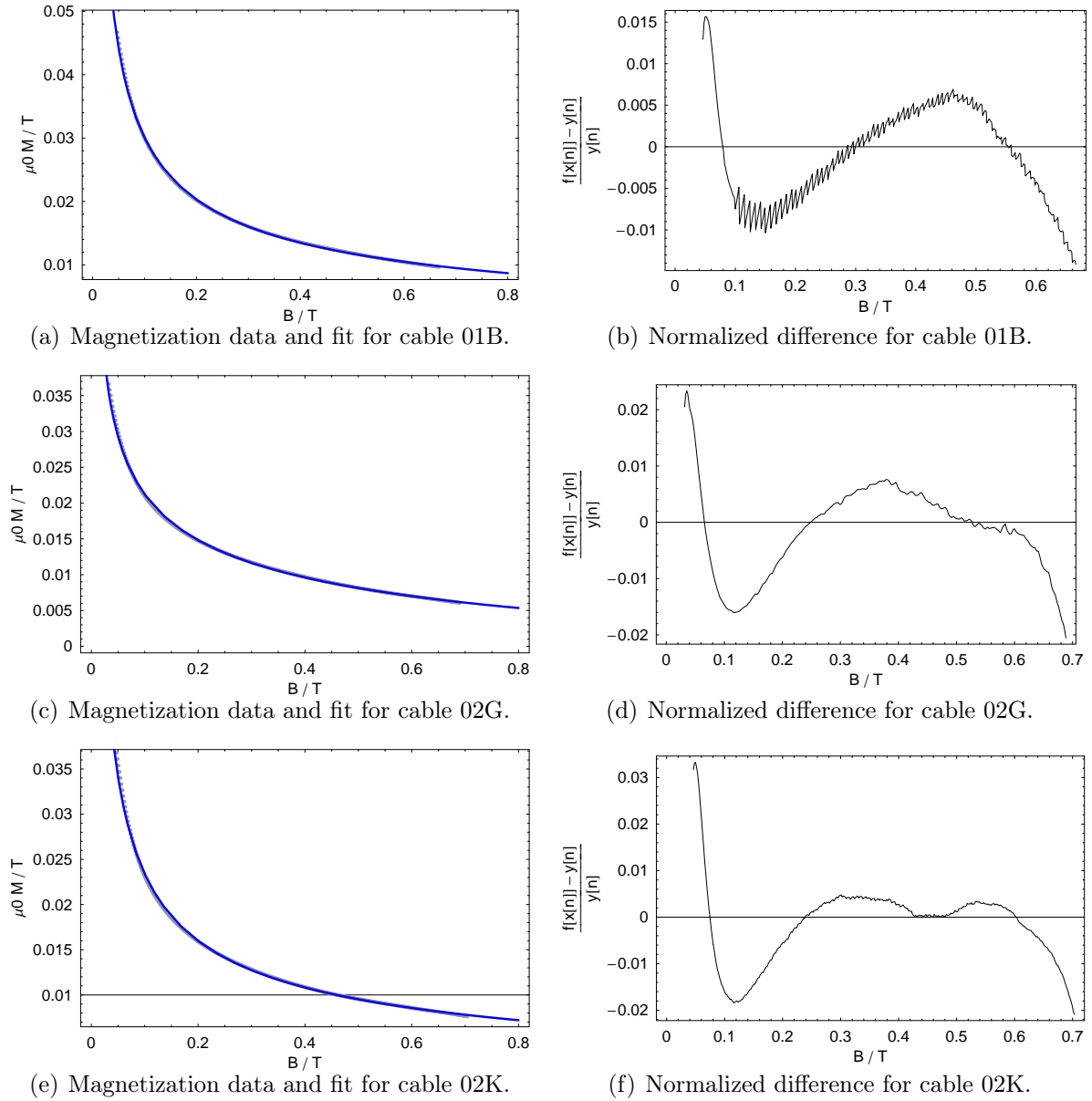
$\beta > 1$ The β dependency is like a parabola and has therefore a slope of 0 at the zero crossing.

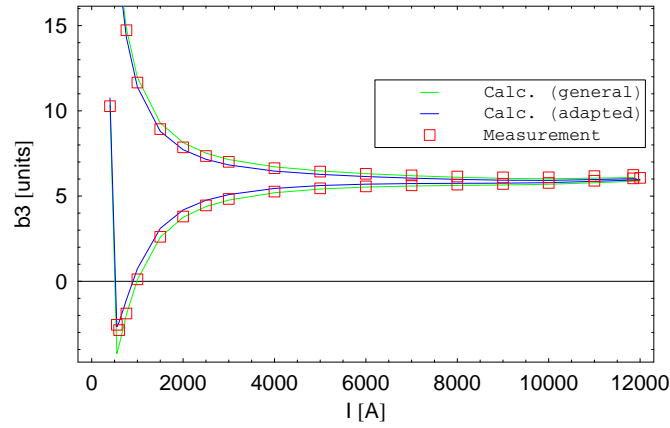
First of all the parabola nature for $\beta > 1$ causes the very small magnetization currents at high field with the small hysteresis loops. This cannot be considered as being correct since the measurements show significantly larger hysteresis widths for high currents.

In general the zero crossing of the critical current density is supposed to be caused by a physical effect which is not expected to change its characteristics from one cable to a similar other one. So the parameter range given in [4] for the scaling power law (see tab. 3.1) has to be adapted and reduced according to the assumed physical effect.

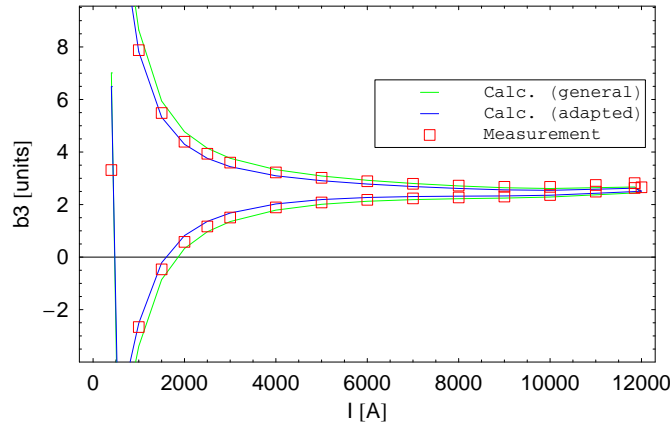
For the moment the characteristic of the transition from superconducting to normal conducting state at the upper critical magnetic induction shall be assumed like in the plots in [7, p. 118f] which shows a steep but finite slope with a soft reducing bending close to zero.

Furthermore for cables with high values of the fit parameter β ($\beta \approx 8$) the critical current density is already for fields of ≈ 4 T of the same magnitude of as transport current density. Cables with such a critical current density could not carry the necessary current corresponding to an excitation of 11800 A and would cause a quench.

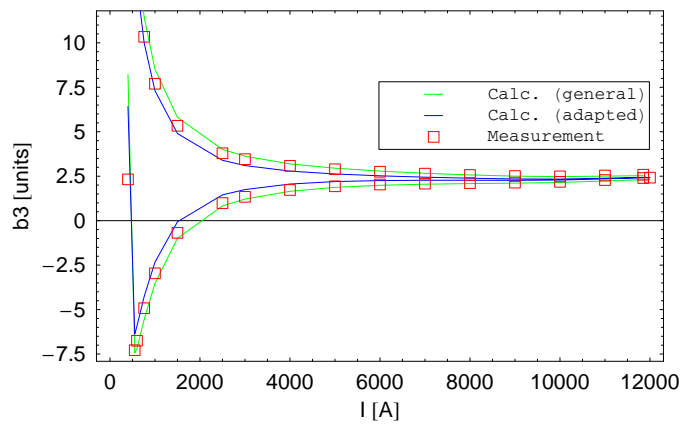
Figure 3.9: Matching of **adapted scaling power law fit** with measurement data.



(a) Magnet number 2009 with coil cross section 1 and cable combination 01B 02C.



(b) Magnet number 3043 with coil cross section 2 and cable combination 01B 02K.



(c) Magnet number 3090 with coil cross section 3 and cable combination 01B 02G.

Figure 3.10: Simulated multipole b_3 for the **adapted scaling power law** compared with cold measurements and the unspecific scaling power law (state of the art).

3.2 Fixed Ending

In order to test the speculations on the effects of the parameter β and the already achieved good results for low currents related to the parameter α , the fit is done with fixed $\beta = 0.9$ and simulated for all shown magnets.

For the calculation of the fit parameter α and $C0$ the measurement data is divided by the β term. Then the method described beforehand can be applied in the same way.

Results for Magnetization

Table 3.5: Parameters and standard deviation for scaling power law with fixed ending.

	01B	01E	02B	02C	02D	02G	02K
α	0.433	0.356	0.380	0.447	0.474	0.422	0.458
β	0.900	0.900	0.900	0.900	0.900	0.900	0.900
$C0$	14.13	12.44	12.24	16.41	14.93	12.07	16.14
$\sigma \cdot 1000$	0.113	0.393	0.134	0.180	0.775	0.720	0.199

The resulting fit function is of less good matching. Especially for the cables with large values for β in section 3.1.3 the deviation between fit function and measured magnetization values is significant. This is indicated by the increased values for the standard deviation σ .

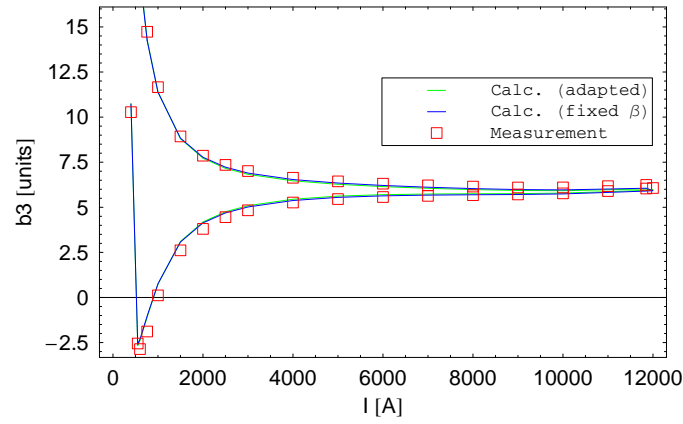
Results for Simulated Magnets

The plots 3.11 a) to c) show the results of the simulation in comparison to the adapted scaling power law approach. Surprisingly the reduction of fit quality has no obvious effect on the simulated multipoles. For low currents the hysteresis loop does not change much. According to the higher critical current density at high field, the hysteresis width increases for high currents but still does not reach the measured values.

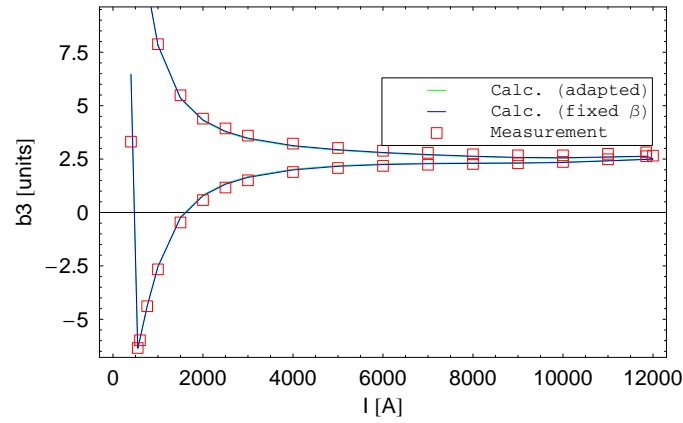
Discussion

The influence of the β term seems to be rather small for low currents if the function is adapted to the measurement via the parameters α and $C0$. For high currents any additional current creates an additional multipole hysteresis width and so the case $\beta < 1$ provides more critical current compared to the parameters determined in section 3.1.3.

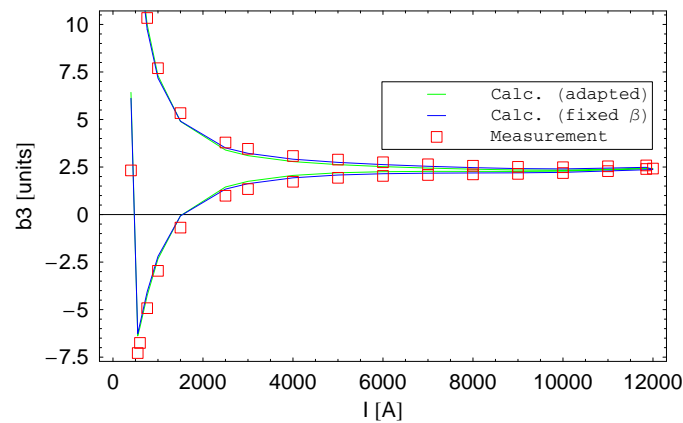
By decreasing the value of β the critical current density could be further increased up to the limit given by $\beta = 0$. Then at the upper critical field B_{c2} the critical current density transits to zero within a step. Since the maximum field of the magnet is in a range of 9 T the β term can be omitted in this.



(a) Magnet number 2009 with coil cross section 1 and cable combination 01B 02C



(b) Magnet number 3043 with coil cross section 2 and cable combination 01B 02K



(c) Magnet number 3090 with coil cross section 3 and cable combination 01B 02G

Figure 3.11: Simulated multipole b_3 for the **scaling power law with fixed ending** compared with cold measurements and the adapted scaling power law.

3.3 Neglecting the Pinch Off

For all latter approaches a term is implemented to pinch off the critical current density at the upper critical field B_{c2} . In a first step it shall be assumed that the effect of the pinch off is small within the range of $0 \rightarrow 8$ T and can be neglected for the LHC cables.

Due to the design of the coil geometry the local magnetic induction differs between all strands and areas of high, medium and low field can be identified. In addition screening and magnetization effects of the filaments cause a further variation of the field distribution. The local magnetic induction in the coil cross section for injection and nominal field is shown in fig. 3.12. It can be seen that although the transportation current is ramped up to 11800 A areas of the coil stay in a field range between $0 \rightarrow 3$ T while others experience a field of up to 8.5 T, depending on their local position within the coil cross section.

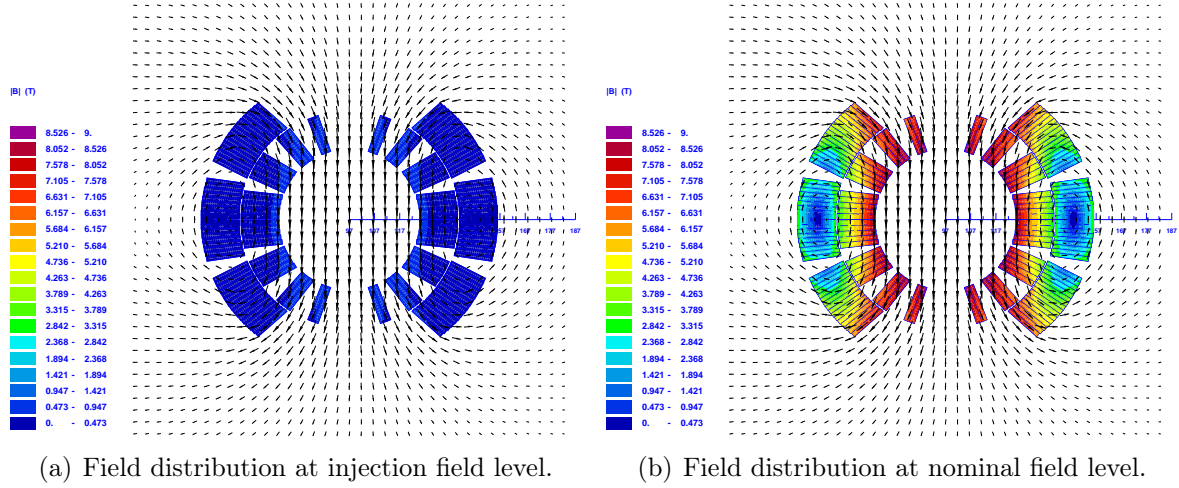


Figure 3.12: Local magnetic induction in the coil cross section. The colors indicate the modulus of the magnetic induction.

For all approaches the critical current density is much higher for low than for high field. Since the effect of one filament on the multipoles in the aperture is related to its position and the amount of magnetization current, these areas of low field will dominate even at nominal field the width of the hysteresis loop although they are situated in the outer layer. As long as the function of critical current density decreases with rising field the influence of the fit function is reduced at the same time. This puts an additional limit to the possibilities of determining the critical current fit function from field error measurements for high field by means of inverse calculation.

Putting together the small influence of high fields and the total field limit of 8.5 T the effects of the pinch off are assumed to be small. So the α part of the function (3.3) seems to be more relevant and yields to:

$$J_c(B, T) = J_{ref} \frac{C0}{B} \left(\frac{B}{B_{c2(T)}} \right)^\alpha \left(1 - \left(\frac{T}{T_{c0}} \right)^n \right)^\gamma \quad (3.5)$$

Results for Magnetization

Table 3.6: Parameters and standard deviation for scaling power law without pinch off term.
By means of the scaling power law fit function the parameter β is set to zero.

	01B	01E	02B	02C	02D	02G	02K
α	0.415	0.337	0.362	0.429	0.456	0.405	0.439
β	0	0	0	0	0	0	0
$C0$	12.87	11.26	11.12	14.90	13.58	11.01	14.65
$\sigma \cdot 1000$	0.157	0.485	0.188	0.255	0.842	0.805	0.171

Compared to the previous approach all values for α and $C0$ decrease. The quality of all fits reduces again except for the cable 02K the fit becomes a little better.

Results for Simulated Magnets

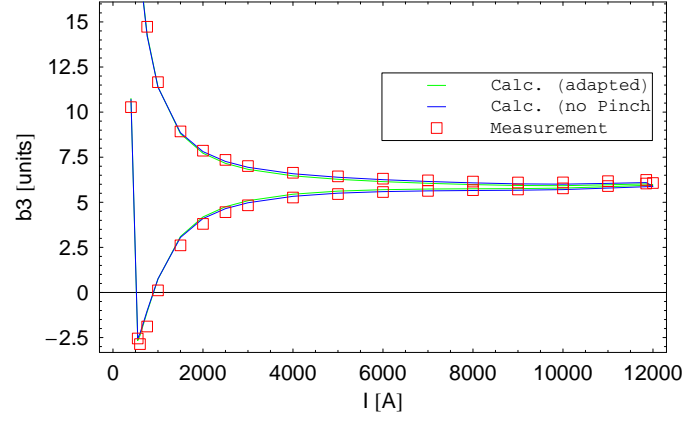
As shown in figs. 3.13 a) to c) the bad matching of the J_c fit curve with the measurement of the magnetization again does not cause a big effect on the field errors in the low current range. For high current the lack of a pinch off gives additional critical current density for high field and therefore increases the width of hysteresis.

Discussion

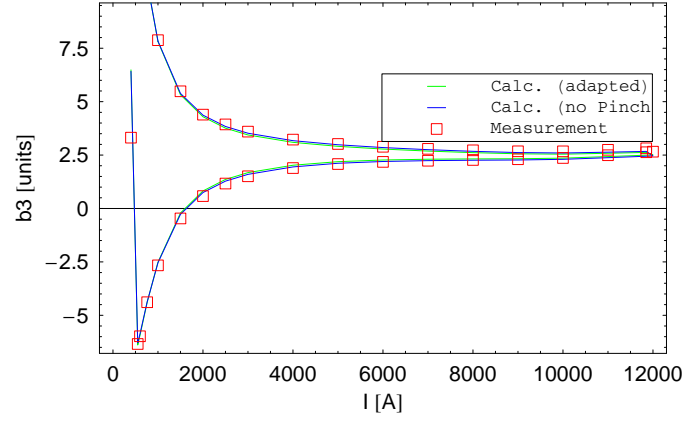
In order to increase the hysteresis width of the field error loop for high currents the critical current density for high field was increased by neglecting the pinch off. The function obtained in this way provides the maximum critical current density at high field by means of the scaling power law approach.

As can be seen from fig. 3.13 the hysteresis loop of the field errors for high currents does not increase significantly and remains much smaller than the measurement. This shows again that the hysteresis width is mainly influenced by the low field part of the critical current density function.

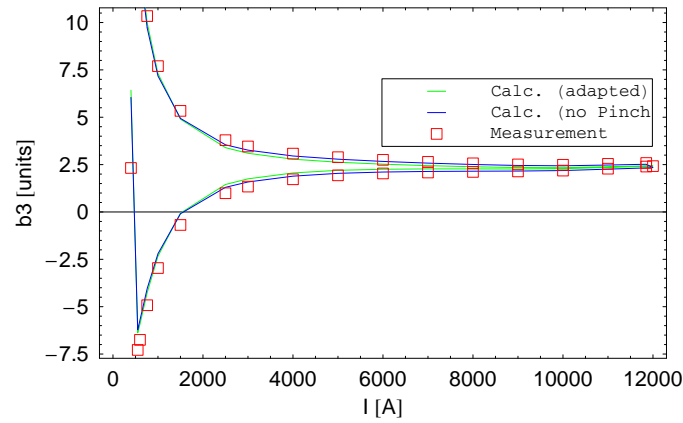
Furthermore it shows that the pinch off is not necessarily needed for the simulation of the main dipole magnet since the local field does not exceed 9 T, if one keeps in mind this limitation. For the more critical case of quench calculation, e.g. at higher temperatures of course a pinch off has to be modeled in order to obtain a physically correct behavior.



(a) Magnet number 2009 with coil cross section 1 and cable combination 01B 02C.



(b) Magnet number 3043 with coil cross section 2 and cable combination 01B 02K.



(c) Magnet number 3090 with coil cross section 3 and cable combination 01B 02G.

Figure 3.13: Simulated multipole b_3 for the **scaling power law approach without pinch off** compared with cold measurements and the adapted scaling power law.

3.4 Double Bending Function

Based on the experience with the scaling power law a new function was invented in order to provide more critical current density in the field range between 1 → 4 T if needed. Therefore the function has been strictly split into a part that models the curve for low fields and is not influencing the part for high field and a part for high field with only a slight influence on the low field range. The major advantage of such a function is that the steering of the high- and low-field parts are separated.

The function given in Eq. (3.6) provides an adjustable bending behavior. In order to describe the special behavior of the new function a characteristic quantity the so-called bend point is defined. The bending point is the threshold where the function is considered as close to one and is without any restriction defined as B_b if $f(B_b) = 1.05$. The bending point can be varied by changing the parameter b . For increasing b the bending point moves towards the ordinate axis. By means of setting the parameter a the slope of the function can be adjusted and the value at zero field is defined. For values of B larger than the bending point the function is always close to 1. In fig. 3.14 a) and b) the influence of the two parameters is demonstrated.

$$f(B) = a \cdot e^{-Bb} + 1. \quad (3.6)$$

For the magnetization measurement data two different slopes and curvatures are distinguishable and therefore the function from Eq. (3.6) is used twice and is coupled in a multiplicative way. The function for low field is given by:

$$f_{low}(B) = (a \cdot e^{-Bb} + 1) (c \cdot e^{-Bd} + 1). \quad (3.7)$$

With the pairs (a, b) and (c, d) the function can be adapted independently to two different curvatures. Figure 3.14 c) shows the combination of two different curvatures.

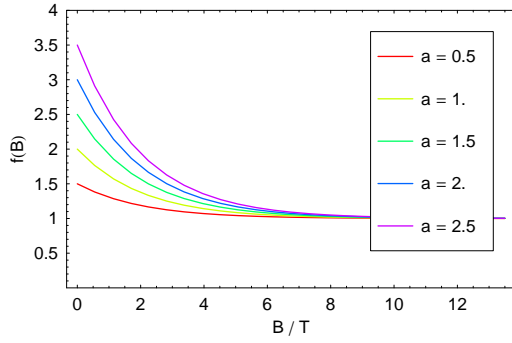
In order to model the pinch off the β term from the sections above is again selected and applied with fixed β value of $\beta = 1.3$, see Eq. (3.8). This provides a good share of critical current density and a horizontal slope only very close to the upper critical field value. Figure 3.14 d) shows the combination of the low and high field part.

$$f_{high}(B) = \left(1 - \frac{B}{B_{c2}}\right)^{1.3}. \quad (3.8)$$

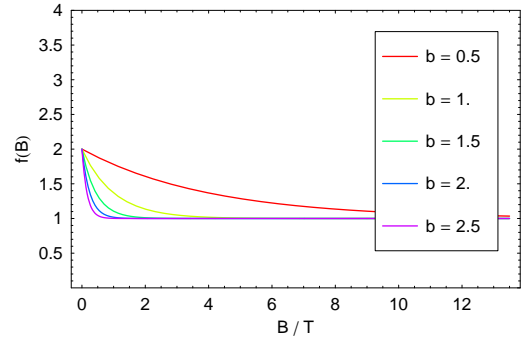
In addition to the temperature dependency of f_{high} the γ term from the scaling power law approach is used. The fit function then is build by the latter three terms, the reference critical current density J_{ref} and a linear constant:

$$J_c(B, T) = J_{ref} C_0 (a \cdot e^{-Bb} + 1) (c \cdot e^{-Bd} + 1) \left(1 - \frac{B}{B_{c2}(T)}\right)^{1.3} \left(1 - \left(\frac{T}{T_{c0}}\right)^n\right)^\gamma. \quad (3.9)$$

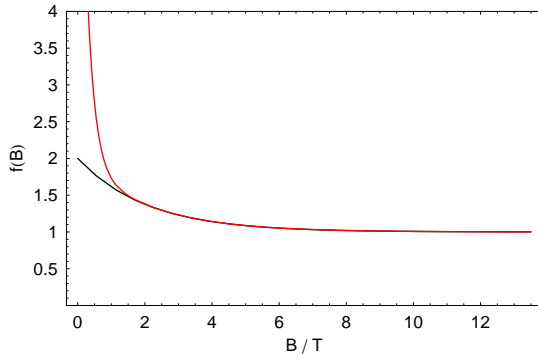
For the determination of the five fit parameters the MATHEMATICA package `NonLinearRegress` was used. Since the function `FindNonLinearFit` can not determine the coefficients of both exponential terms simultaneously the parameters a and b have been determined manually.



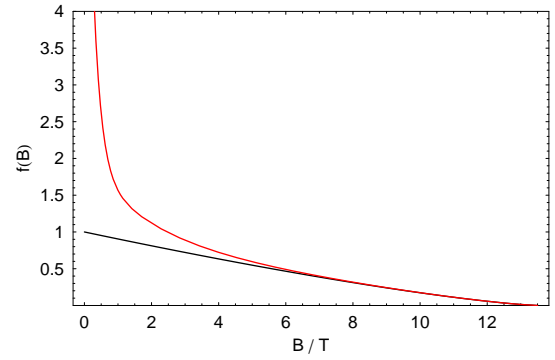
(a) Influence of the parameter a . The slope and the value of the function can be determined by the parameter a .



(b) Influence of the parameter b . The rising point can be determined by the parameter b .



(c) Combination of two curvatures with two sets of parameters. The black curve shows the function with the smaller curvature which is combined to the red curve.



(d) In addition to the combination of two different curvatures as in c) the model of the pinch off indicated by the black line is included.

Figure 3.14: The double bending function shown in different steps of development.

Results for Magnetization

Table 3.7: Parameters and standard deviation for the double bending function. The parameter β is kept constant to $\beta = 1.3$. For the parameters a and b only values of 3 digits have been tested.

	01B	01E	02B	02C	02D	02G	02K
$C0$	4.290	4.506	4.077	4.518	3.941	3.215	4.480
a	3.00	3.30	3.40	3.10	3.55	4.50	2.95
b	3.20	3.00	3.00	3.00	3.50	3.20	3.15
c	1.725	1.414	1.991	1.479	1.063	1.403	2.000
d	19.87	12.55	17.90	18.80	32.62	25.36	23.37
$\sigma \cdot 1000$	0.094	0.091	0.083	0.075	0.083	0.065	0.095

As can be seen from tab. 3.7 the matching of the double bending function on the measured magnetization data is for all cables much better than for the previous approaches. In addition all parameters stay in a similar magnitude which indicates the general usability of the fit for all measured NbTi cables.

In fig. 3.15 the matching of the fit function with the magnetization data for the same three cables as in fig. 3.9 is shown. The normalized differences for the double bending function fit is for each cable smaller than for the adapted scaling power law by approximately the factor 2.

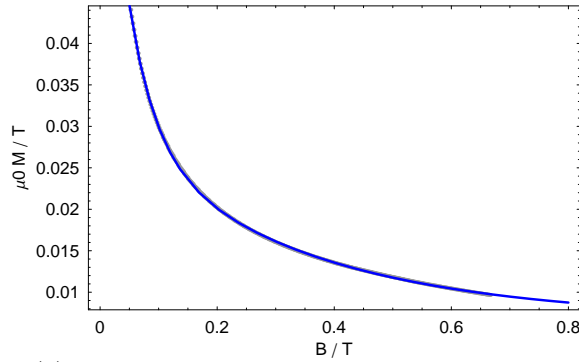
Results for Simulated Magnets

The simulation results of the multipole b_3 shown in figs. 3.16 a) to c) give for low and high currents a very good matching although the simulated values for low currents are slightly smaller than those obtained from the adapted scaling power law (not shown in the plot).

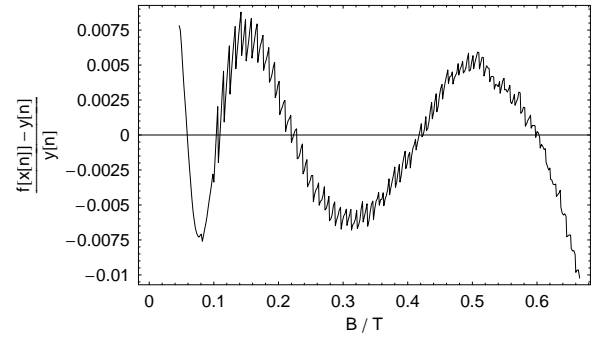
Discussion

The new double bending function differs from the other approaches since it does not give infinite values for zero field. Like the measurement of magnetization it shows for zero field finite values. For a real cable an unknown limiting effect is assumed to cause the finite values at zero field, but this does not reduce the physical probability of the new function. An option would be to model the branch of magnetization separately by additional bending terms down to zero field.

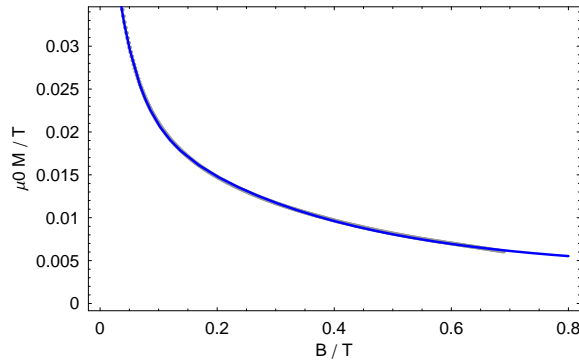
The temperature dependency is for the moment only included in the β and the γ terms. Further investigations could motivate the need of a temperature dependency of the function (3.6) which could be included either in the parameter a , the parameter b or both.



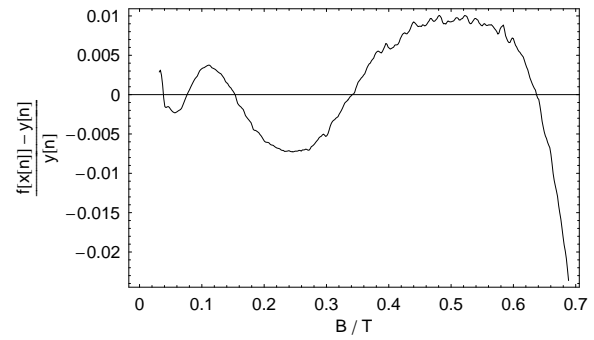
(a) Magnetization data and fit for cable 01B.



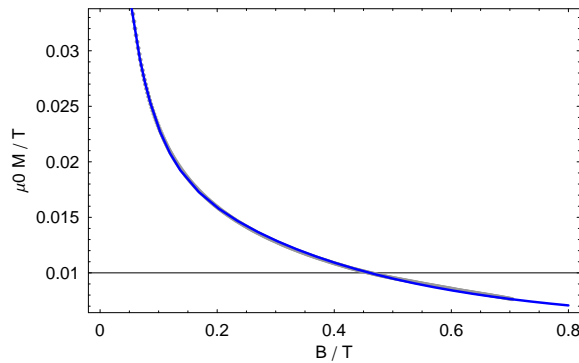
(b) Normalized difference for cable 01B.



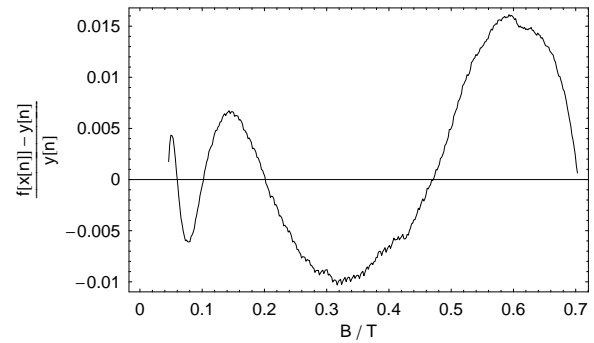
(c) Magnetization data and fit for cable 02G.



(d) Normalized difference for cable 02G.

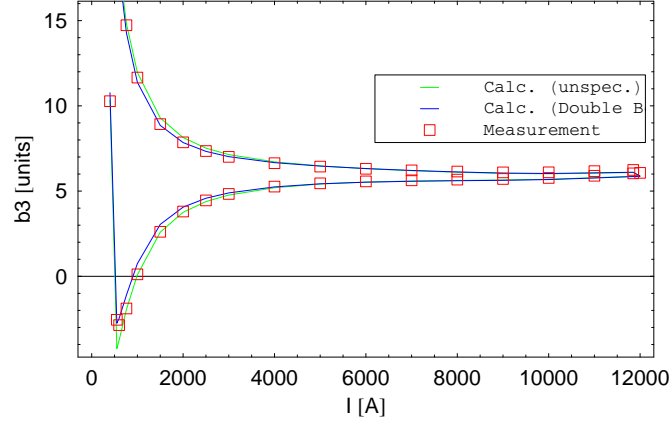


(e) Magnetization data and fit for cable 02K.

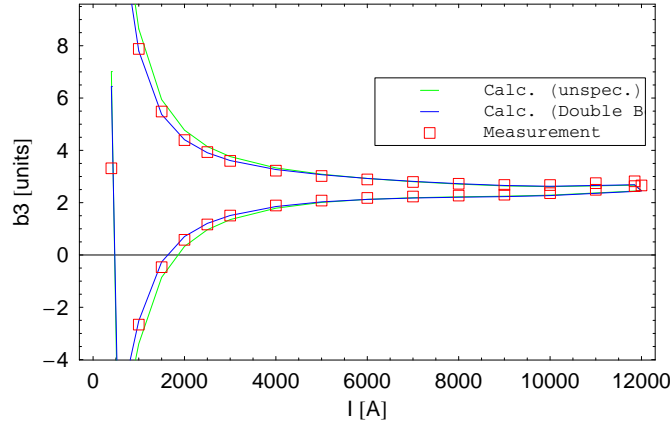


(f) Normalized difference for cable 02K.

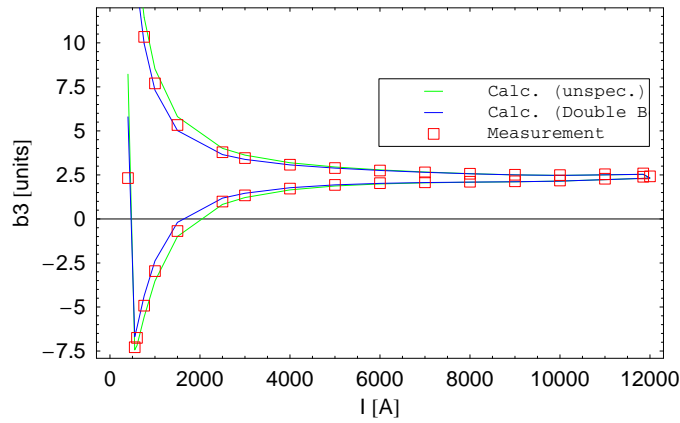
Figure 3.15: Matching of the **double bending function fit** with measurement data.



(a) Magnet number 2009 with coil cross section 1 and cable combination 01B 02C.



(b) Magnet number 3043 with coil cross section 2 and cable combination 01B 02K.



(c) Magnet number 3090 with coil cross section 3 and cable combination 01B 02G.

Figure 3.16: Simulated multipole b_3 for the **double bending approach** compared with cold measurements and the unspecific scaling power law (state of the art).

4 Conclusion and Outlook

4.1 Conclusion

The influence of the different fit functions on the field errors in the aperture of the superconducting LHC main dipole magnets is analyzed. It can be seen that the influence of the fit function on the magnetic multipoles differs for low and high currents and therefore these two ranges are discussed separately.

For small excitation currents the simulation results of all adapted approaches show very similar multipole errors. The varying quality of the fits on the magnetization data, which is indicated by the value σ , can not be observed from the multipole errors. As one can see from fig. 4.1 the values of all adapted fit functions are very close to each other and only start to differ for values of the magnetic induction higher than 1 T.

The double bending fit function gives the best fit according to the σ value therefore best represents the measured magnetization.

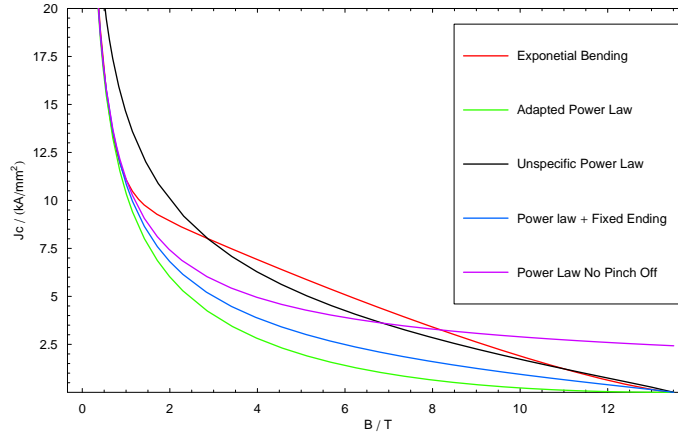


Figure 4.1: All fit functions used within this thesis adapted for the inner cable 01B. For small field values all adapted functions are very similar. For high field values the functions differ significantly in the provided critical current density.

For high currents the hysteresis width of the multipoles differs heavily depending on the used fit function. The hysteresis width is strongly influenced by the amount of critical current density provided by the fit function in the field range of $1 \rightarrow 4$ T.

The adapted scaling power law approach gives very small critical current density for high currents due to the high values of the parameter β . In addition to the small hysteresis width

this might cause further problems because the critical current density and the transport current density reach of the same order of magnitude for high field and high transport current. This is not foreseen in the model and would strongly influence the induced field errors due to the sharing of available current amongst the two parties. For high values of β the cable should cause a quench within the operation field range what is not observed.

For the approach with the fixed ending the critical current density is increased due to the small value for the parameter β but still does not increase the hysteresis width. Even for the approach which neglects the pinch off at the upper critical induction B_{c2} and therefore provides the maximum critical current density at high fields in respect to all functions of the scaling power law type, the hysteresis width is not sufficiently increased.

The double bending function with the used exponent of 1.3 provides already enough critical current density to match the measured hysteresis width. In addition, this parameter can be changed if necessary.

Figure 4.1 shows all fit functions used for the inner cable 01B and also shows the different amount of critical current density for high field values for all fit functions. The fit functions only differ significantly in the range where no magnetization data is available.

In general the used fit function in the given parameter range should be of the same kind for all NbTi cables since they are all of the same type thus following the same physical principles and differences are only resulting from the production process. The behavior for field values close to zero and close to the upper critical field B_{c2} must not change. For this reason the scaling power law is considered to be critical if values for the parameter β smaller **and** bigger than 1 are allowed.

From the author's point of view the needed parameter range to fit all different cable sufficiently is a further indicator for the quality of the fit since cables with exceeding parameter ranges seem to be of different type.

To put it in a nutshell the **new type double bending fit function** represents best the magnetization data and does not show any physical or structural deviations and therefore is considered to be most appropriate for the simulation of the LHC main dipole magnets.

4.2 Outlook

For this thesis the slight difference between the rising and falling part of the superconductor magnetization hysteresis loop was neglected and the fit was carried out for the falling upper branch only. In some cases this is slightly imprecise as can be seen from the measured values. Thus, the effect of a separate fit which is triggered for each branch could be investigated. A magnetization measurement is needed which provides a field ramp from the positive to the negative and back to the positive maximum field in order to obtain also a fully penetrated specimen for the lower branch at zero field.

If one could model the small Meissner-phase separately, the effects to be modeled reduce and the fit function should become less complex.

The observed strong influence of the critical current density for high field on the hysteresis width at high excitation currents gives strong arguments to extend the field range of the

magnetization measurement up to 8 T or at least 4 T in order to support the high field term more precisely.

For the new double bending fit function the temperature dependency has to be investigated. This was no objective of this thesis and the already applied dependency might not describe the real behavior suitably enough to perform a quench analysis or to carry out calculations for different temperatures.

The high field term of the double bending function could undergo a further development especially in order to fix the behavior for the transition from superconducting to normal conducting state at the upper critical field.

In order to model the critical current density for a magnetic induction close to zero further bending function parts could be considered. The function then could be applied in the following form:

$$J_c(B) = J_{ref} C_0 \prod_{n=1}^N (a_n \cdot e^{-B b_n} + 1) f_{high}(B).$$

Bibliography

- [1] Charles P. Bean. Magnetization of High Field Superconductors. *Review of Modern Physics*, 36:31–39, 1964.
- [2] B. Bellesia, L. Bottura, V. Granata, S. Le Naour, L. Oberli, S. Sanfilippo, C. Santoni, W. Scandale, N. Schwerg, E. Todesco, and C. Vollinger. Trends in Cable Magnetization and Persistent Currents during the Production of the Main Dipoles of the Large Hadron Collider, 2005. (LHC Note - to be published).
- [3] J. Billan, L. Bottura, M. Buzio, G. D’Angelo, G. Deferne, O. Dunkel, P. Legrand, A. Rijllart, A. Siemko, P. Sievers, S. Schloss, and L. Walckiers. Twin Rotating Coils for Cold Magnetic Measurements of 15 m Long LHC Dipoles. In *16th International Conference on Magnetic Technology*, Ponte Vedra Beach, USA, 1999.
- [4] L. Bottura. A Practical Fit for the Critical Surface of NbTi. In *16th International Conference on Magnetic Technology*, Ponte Vedra Beach, USA, 1999.
- [5] Oliver Brüning, P. Collier, P. Lebrun, S. Myers, R. Ostojic, J. Poole, and P. Proudlock, editors. *LHC design report - vol.1 the LHC main ring*. CERN, Geneva, Switzerland, 2004.
- [6] Werner Buckel. *Supraleitung*. VCH, Weinheim, Germany, 1994.
- [7] E W Collings. *Applied superconductivity, metallurgy, and physics of titanium alloys*, volume 2. Plenum Publishing Corporation, New York, USA, 1986.
- [8] N. R. Draper and H. Smith. *Applied Regression Analysis*. John Wiley & Sons, Inc, 1966.
- [9] Michael A. Green. Generation of the J_c , H_c , T_c Surface for Commercial Superconductor Using Reduced-State Parameters, 1988.
- [10] S. Le Naour, L. Oberli, R. Wolf, R. Puzniak, A. Szewczyk, A. Wisniewski, H. Fikis, M. Foitl, and H. Kirchmayr. Magnetization Measurements on LHC Superconducting Strands. In *Applied Superconductivity Conference*, Palm Springs, USA, 1998.
- [11] S. Le Naour, R. Wolf, J. Billan, and J. Genest. Test Station for Magnetization Measurements on Large Quantities of Superconducting Strands. In *Applied Superconductivity Conference*, Virginia Beach, USA, 2000.

-
- [12] P. Lefèvre and T. Pettersson, editors. *The Large Hadron Collider - Conceptual Design*. CERN, Geneva, Switzerland, 1995.
 - [13] M. S. Lubell. Empirical Scaling Formulas for Critical Current and Critical Field for Commercial NbTi. *IEEE Transactions on Magnetics*, MAG-19(2), May 1983.
 - [14] K.-H. Mess, P. Schmüsser, and S. Wolff. *Superconducting Accelerator Magnets*. World Scientific, 1996.
 - [15] S. Russenschuck. *Electromagnetic Design and Optimization of Accelerator Magnets*. CERN, 2004. (to be published).
 - [16] S. Sanfilippo. Do you really want to test them all at cold? In *LHC days 2003*, Les Diablerets, France, 2003.
 - [17] S. Sanfilippo, A. Akhmetov, L. Bottura, M. Buzio, M. Gateau, F. Patru, N. Smirnov, and L. Walckiers. Magnetic Measurements for 15 m long dipoles - Standard Program of Cold Test, 2001. LHC-MTA-IN-2001-169.
 - [18] L. T. Summers. A Model for the Prediction of Nb_3Sn Critical Current as Function of Field, Temperature, Strain, and Radiation Damage. *IEEE Transactions on Magnetics*, 27(2), March 1991.
 - [19] C. Völlinger. *Superconductor Magnetization Modeling for the Numerical Calculation of Field Errors in Accelerator Magnets*. PhD thesis, Technische Universität Berlin, 2003.
 - [20] K. Wille. *Physik der Teilchenbeschleuniger und Synchrotronstrahlungsquellen*. Teubner, 1996.
 - [21] Martin N. Wilson. *Superconducting Magnets*. Monographs on Cryogenics, Oxford University Press, New York, USA, 1983.

A Intersecting Circles

Considering a geometry of two circular cylinders of equal but opposite current density J intersecting as shown in fig. A.1 yields a current free region of homogeneous field in the overlapping area.

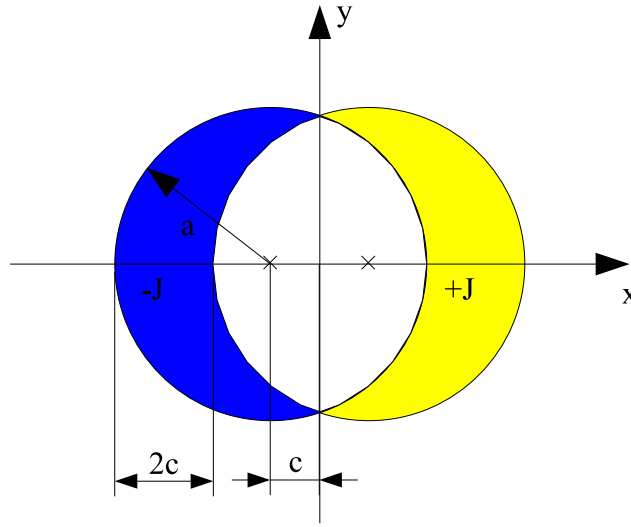


Figure A.1: Geometry of two intersecting circles.

The field of magnetic induction of one cylinder with radius a and homogeneous current density J can be calculated by OERSTEDTS law and yields

$$B_{\phi}(\rho) = \frac{\mu_0 J a}{2} \begin{cases} \rho/a & \rho \leq a \\ a/\rho & \rho > a \end{cases} \quad (\text{A.1})$$

Using

$$\begin{aligned} \rho &= \sqrt{x^2 + y^2} \\ \vec{e}_{\phi} &= -\sin \phi \vec{e}_x + \cos \phi \vec{e}_y \\ &= -\frac{y}{\sqrt{x^2 + y^2}} \vec{e}_x + \frac{x}{\sqrt{x^2 + y^2}} \vec{e}_y \end{aligned}$$

this can be transformed in to Cartesian coordinates yielding:

$$\vec{B}(x, y) = \frac{\mu_0 J a}{2} \begin{cases} -\frac{y}{a} \vec{e}_x + \frac{x}{a} \vec{e}_y & \sqrt{x^2 + y^2} \leq a \\ a \left(-\frac{y}{x^2 + y^2} \vec{e}_x + \frac{x}{x^2 + y^2} \vec{e}_y \right) & \sqrt{x^2 + y^2} > a \end{cases} \quad (\text{A.2})$$

Superposing the fields of two cylinders shifted by the length c yields the field of the intersecting geometry and shall be shown for the overlapping part only:

$$\begin{aligned}\vec{B}(x, y) &= \vec{B}(x - c) - \vec{B}(x + c) \\ &= -\mu_0 J c \vec{e}_y\end{aligned}\tag{A.3}$$

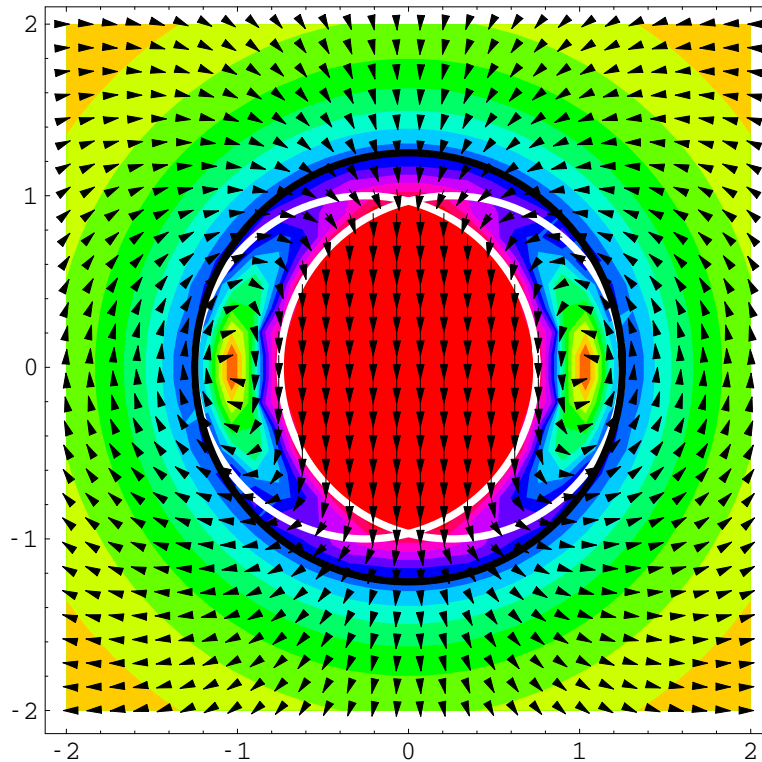


Figure A.2: Field of two intersecting cylinders.

B Mathematical Tools

B.1 Standard Deviation

The standard deviation σ is usually used for statistical statements about hypotheses but for the above context it should be used to give a numerical grade of match for the fit function and the simulation results.

$$\sigma = \sqrt{\frac{1}{I} \sum_{i=1}^I (y_i - f(x_i))^2} \quad (\text{B.1})$$

Being x_i and y_i one pair of a dataset of length I and $f(x_i)$ is usually denoted the hypothesis at x_i .

B.2 Linear Regression

The method of linear regression [8] is a perfect way to assign parameters of a fit function which can be written as sum of different functions and does not contain fit parameters in its argument. The main idea is to minimize the distance between a given set of values and an approximation. Therefore the standard deviation (see B.1), which gives kind of an Euclidian norm, could be calculated and analytically minimized by setting the first derivative to zero.

The fit function $F(x)$ may be given by

$$F(x) = \sum_{n=1}^N a_n f_n(x) \quad (\text{B.2})$$

with a_n the coefficients and f_n the elementary parts. In order to find the best parameters a_n the fit function is put into the standard deviation (B.1). Since the number of data I is constant for one set of data and the root function is absolute monotone both can be omitted with out changing the localisation of the minimum.

$$\min \left(\sqrt{\frac{1}{I} \sum_{i=1}^I (y_i - F(x))^2} \right) = \min \left(\sum_{i=1}^I (y_i - F(x))^2 \right)$$

Applying the N -dimensional gradient operator $\vec{\nabla}_{a_n} \cdot (\dots)$ of the parameter vector space to the term yields a linear equation with the a_n as coefficients of the solutional vector.

$$\begin{aligned}
\vec{0} &= \vec{\nabla}_{a_n} \cdot \left(\sum_{i=1}^I (y_i - F(x))^2 \right) \\
\iff \vec{0} &= \sum_{i=1}^I (y_i - F(x_i)) \begin{pmatrix} f_1(x_i) \\ \vdots \\ f_N(x_i) \end{pmatrix} \\
\iff \sum_{i=1}^I y_i \begin{pmatrix} f_1(x_i) \\ \vdots \\ f_N(x_i) \end{pmatrix} &= \sum_{i=1}^I \left(\sum_{n=1}^N a_n f_n(x_i) \right) \begin{pmatrix} f_1(x_i) \\ \vdots \\ f_N(x_i) \end{pmatrix} \\
\iff \begin{pmatrix} \sum_{i=1}^I y_i f_1(x_i) \\ \vdots \\ \sum_{i=1}^I y_i f_N(x_i) \end{pmatrix} &= \begin{pmatrix} \sum_{i=1}^I f_1(x_i)^2 & \cdots & \sum_{i=1}^I f_1(x_i) f_N(x_i) \\ \vdots & \ddots & \vdots \\ \sum_{i=1}^I f_N(x_i) f_1(x_i) & \cdots & \sum_{i=1}^I f_N(x_i)^2 \end{pmatrix} \begin{pmatrix} a_1 \\ \vdots \\ a_N \end{pmatrix}
\end{aligned}$$

This inhomogeneous linear equation with symmetric matrix shall be written for simplicity reasons as

$$\vec{b} = \underline{\mathbf{M}} \vec{a} \quad (\text{B.3})$$

with

$$\begin{aligned}
\underline{\mathbf{M}} &= (m_{k,l})_{N,N} \\
m_{k,l} &= \sum_{i=1}^I f_k(x_i) f_l(x_i) \\
b_k &= \sum_{i=1}^I y_i f_k(x_i)
\end{aligned}$$

Finally the optimal parameters are given by

$$\vec{a} = \underline{\mathbf{M}}^{-1} \vec{b} \quad (\text{B.4})$$

From the mathematical point of view the solvability of the system can not be determined, but the situation from which the system has been derived gives strong arguments for a certain solvability.